AFRL-ML-WP-TM-2003-4099

NONDESTRUCTIVE EVALUATION (NDE) TECHNOLOGY INITIATIVES
Delivery Order 0031: Modeling of Eddy Current Array Sensor Sensitivities

John R. Bowler

Iowa State University
Center for Nondestructive Evaluation
Applied Sciences Complex II
1915 Scholl Road
Ames, IA 50011

OCTOBER 2002

Final Report for 26 November 2001 – 31 October 2002

MATERIALS AND MANUFACTURING DIRECTORATE
AIR FORCE RESEARCH LABORATORY
AIR FORCE MATERIEL COMMAND
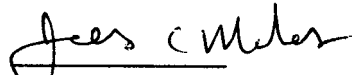**WRIGHT-PATTERSON AIR FORCE BASE, OH 45433-7750**

NOTICE

WHEN GOVERNMENT DRAWINGS, SPECIFICATIONS, OR OTHER DATA INCLUDED IN THIS DOCUMENT FOR ANY PURPOSE OTHER THAN GOVERNMENT-RELATED PROCUREMENT DOES NOT IN ANY WAY OBLIGATE THE US GOVERNMENT. THE FACT THAT THE GOVERNMENT FORMULATED OR SUPPLIED THE DRAWINGS, SPECIFICATIONS, OR OTHER DATA DOES NOT LICENSE THE HOLDER OR ANY OTHER PERSON OR CORPORATION, OR CONVEY ANY RIGHTS OR PERMISSION TO MANUFACTURE, USE, OR SELL ANY PATENTED INVENTION THAT MAY RELATE TO THEM.

THIS REPORT IS RELEASABLE TO THE NATIONAL TECHNICAL INFORMATION SERVICE (NTIS). AT NTIS, IT WILL BE AVAILABLE TO THE GENERAL PUBLIC, INCLUDING FOREIGN NATIONS.

THIS TECHNICAL REPORT HAS BEEN REVIEWED AND IS APPROVED FOR PUBLICATION.

JUAN G. CALZADA, Project Engineer
Nondestructive Evaluations Branch
Metals, Ceramics & NDE Division

JAMES C. MALAS, Chief
Nondestructive Evaluations Branch
Metals, Ceramics & NDE Division

GERALD J. PETRAK, Assistant Chief
Metals, Ceramics & NDE Division
Materials & Manufacturing Directorate

DO NOT RETURN COPIES OF THIS REPORT UNLESS CONTRACTUAL OBLIGATIONS OR NOTICE ON A SPECIFIC DOCUMENT REQUIRES ITS RETURN.

REPORT DOCUMENTATION PAGE

1. REPORT DATE *(DD-MM-YY)*	2. REPORT TYPE	3. DATES COVERED *(From - To)*
October 2002	Final	11/26/2001 – 10/31/2002

4. TITLE AND SUBTITLE		5a. CONTRACT NUMBER
NONDESTRUCTIVE EVALUATION (NDE) TECHNOLOGY INITIATIVES		F33615-97-D-5271
Delivery Order 0031: Modeling of Eddy Current Array Sensor Sensitivities		5b. GRANT NUMBER
		5c. PROGRAM ELEMENT NUMBER
		62102F
6. AUTHOR(S)		**5d. PROJECT NUMBER**
John R. Bowler		4349
		5e. TASK NUMBER
		40
		5f. WORK UNIT NUMBER
		01

7. PERFORMING ORGANIZATION NAME(S) AND ADDRESS(ES)	8. PERFORMING ORGANIZATION REPORT NUMBER
Iowa State University Center for Nondestructive Evaluation Applied Sciences Complex II 1915 Scholl Road Ames, IA 50011	

9. SPONSORING/MONITORING AGENCY NAME(S) AND ADDRESS(ES)	10. SPONSORING/MONITORING AGENCY ACRONYM(S)
Materials and Manufacturing Directorate Air Force Research Laboratory Air Force Materiel Command Wright-Patterson AFB, OH 45433-7750	AFRL/MLLP
	11. SPONSORING/MONITORING AGENCY REPORT NUMBER(S) AFRL-ML-WP-TM-2003-4099

12. DISTRIBUTION/AVAILABILITY STATEMENT

Approved for public release; distribution is unlimited.

13. SUPPLEMENTARY NOTES

Report contains color.

14. ABSTRACT

A computer simulation has been developed to evaluate eddy-current probes containing magnetic field sensor arrays for the detection and evaluation of hidden corrosion. The simulation is used to assess probes that incorporate magneto-resistive or Hall devices in a closely spaced, linear array. These probes will allow rapid data acquisition over a track width determined by the length of the array. The benefit of the simulation is that adjustments to the virtual probe parameters are easily made, allowing improvements in sensitivity, imaging capability, and resolution. A number of probe designs have been studied in this way, including the racetrack probe. A numerical model for finding the unknown dipole density inside the flaw region has been developed. The analysis is based on the curl of edge elements for representing the dipole density and use of Galerkin's method for evaluating the unknowns. Tree-cotree decomposition is used to reduce the problem complexity.

15. SUBJECT TERMS

eddy current, giant magneto resistive (GMR) sensors, edge elements techniques, Dyadic Green's function formulations

16. SECURITY CLASSIFICATION OF:			17. LIMITATION OF ABSTRACT:	18. NUMBER OF PAGES	19a. NAME OF RESPONSIBLE PERSON (Monitor)
a. REPORT	**b. ABSTRACT**	**c. THIS PAGE**	SAR	74	Juan Calzada
Unclassified	Unclassified	Unclassified			**19b. TELEPHONE NUMBER** *(Include Area Code)* (937) 255-1605

Contents

Preface

Following an initial phase of work in which a simulation of eddy current corrosion detection for idealized structures was developed, this report covers Phase II of the project in which the objective is refine the numerical model to simulate inspections taking into account complex structural features found on aircraft.

In the foundation phase of the work, the main objective was to produce a measurement model for basic layered structures of infinite transverse extent containing local, regular or irregular flaws representing material loss due to corrosion. The model determines the magnetic field at any point above the metal structure and can therefore predict measurements made by giant magneto resistive (GMR) sensors or Hall devices. The output of the model was validated by comparisons with experimental measurements of probe impedance and sensor signals due to material loss in conducting plates. The objectives of the first phase were achieved. In addition, a study was made of a specific array probe concept based on the racetrack coil. The coil shape is similar in plan view to that of a running track with semi-circular bends connected by straight sections. The work on the racetrack coils is described in an article submitted to Journal of Applied Physics and is reproduced in this report. Also in the foundation phase, initial steps were taken to investigate the effectiveness of sensor array probes for the detection of roughness on hidden surfaces.

Eddy current measurements on aircraft give large indications due to fasteners and other structural features such as the edge of a plate in a lap joint. It is often the case that flaw detection is hampered because the effects of normal structure masks the signal due to the defect. Because of their significance in the detection and evaluation of flaws, the simulation has been extended to take account of the two basic structural features, fasteners and lap joints. In order to produce a reliable simulation code for this task, a new numerical scheme has been developed in partnership with Dr's Guglielmo Rubinacci and Antonello Tamburrino from the University of Cassino, in Italy.[a]

This partnership enable us to build on our combined experience of two approaches to the design of numerical code. The Cassino group has been prominent in the use of edge elements techniques and Dr John Bowler at CNDE has developed numerical techniques based on dyadic Green's function formulations. Features of these two approaches have been forged together to produce a new formulation with the aim exploiting the advantages of each.

In parallel with the design of a new numerical scheme, experiments have been carried out to validate model predictions. The measurements are made using probes consisting of a calibrated Hall sensor located on the axis of a circular drive coil. Although this is not an array probe, it has the advantage that it can be well characterized for modelling and code validation purposes. The aim of the validation work is to check that the simulation predicts accurate results for probe signals due to an isolated fastener and an elementary lap joint.

---

[a]Cassino is known for the famous World War II battle of Monte Cassino which preceded the fall of Rome.

Summary

The central task of Phase II is to reconfigure the numerical scheme using edge elements. The motivation for this is that the array probe simulation is then based on an approach that is more reliable and efficient than the previous method based on traditional volume elements. With an improved algorithm, calculation of the electromagnetic field in such structure as a fastener or a lap joint can be performed faster because the underlying computational engine uses as few unknown as possible and is more reliable because it is constructed in such a way as to avoid spurious modes.

In fact the numerical approach that represents the field in terms of edge elements, was develop over the last decade to overcome the problem of spurious solutions. The group at Cassino, who participated in the present project, were at the forefront of this effort and we are fortunate that they could partner with CNDE to create a computational scheme that, when fully developed, will be at the forefront of modern numerical techniques.

Due to delays in finalizing the agreement between Iowa State University and Cassino, the work on the new numerical formulation was not completed until August which left little time for coding. However, Vipul Katyal has work hard on the prototype of the new code at ISU, and initial tests for bugs accuracy and performance have been carried out. Further work is needed before the code is validated and can be used for routine calculations.

Improvement in the experimental methods for validation have been made by using a Stanford lock-in analyzer for magnetic sensors measurements. New probes have been built for the Phase II validation work with an improve signal to noise performance. Because the measuring systems has been upgraded, new measurements have been performed on specimens manufactured in the first year of this project and some new test pieces added.

This report is divided into a series of articles beginning with a summary of some numerical and experimental results. This is followed by a brief account of a proposed imaging method for assessing material loss and Article 3 is a copy of a paper on the racetrack coil submitted to Journal of Applied Physics. In addition we have included a technical review of dyadic Green's functions for layered structures, Article 4, which was written to coordinate theoretical developments at Cassino and ISU. Finally we include a comprehensive report from Rubinacci and Taburrino giving the edge element theory and an outline of the new numerical formulation.

Article 1

Simulation of Eddy Current Array Probes: Predictions and Measurements

1.1   Introduction

In this project we have developed a computer simulation of eddy-current inspection of layered structures using probes containing giant magneto-resistive (GMR) or other solid state sensors for detecting material loss and surface roughness due to corrosion. Experiments have been performed to validate the simulation by comparing predictions of the magnetic field with experimental measurements performed using calibrated Hall devices. The field calculation treats the sensors as independent and therefore only requires validation using single sensor probes.

Conventional driver pick-up eddy current probes use an induction coil to induce current in the part and a pick-up coil to sense perturbation in the field due to flaws. Having a magnetic field sensor, such as a magneto-resistor (MR) or Hall device, instead of the pick-up coil means that the sensitivity of the field measurement is maintained at low frequency and the spatial resolution is high because the field sensitive area in the sensor is usually less than a millimeter across. There may be more intrinsic noise generated by a solid state sensor than by a pick-up coil but intrinsic noise is negligible compared with extrinsic noise due to surface roughness, material variations, scanning irregularities and so on. The main benefit of solid state sensors is the low frequency sensitivity leading to improved detection of subsurface flaws.

In this article, numerical predictions of magnetic field sensor measurements are summarized and calculations are compared with experimental measurements to validate the simulations. The conclusion reviews the need to quantify corrosion damage using array probe data. Specifically through assessment of material loss and the measurement of surface roughness. This implies that new inversion tools are needed. In addition, it is evident that the images of corrosion, do not necessarily match up to the shape of the corroded area. Hence there is a need for image processing tools to improve the visualization of damaged regions. Article 2 makes a start on addressing this issue by showing how a corroded region may be imaged quantitatively using traditional signal processing methods. In this article, a brief report is given of some specific numerical results and validation experiments for loss regions, holes, fasteners and lap joints.

1.2   Numerical Predictions and Experimental Results

Experiments have been performed using probes consisting of a circular coil and a Hall sensor located on the coil axis, Figure 1. The sensor measures the magnetic field component in the axial direction, perpendicular to the surface of the conductor. Two types of sensor types are used in the probes. One is a Honeywell silicon device, 634SS2, in a dual in-line plastic package which contains a preamplifier. The other, made by Asahi Kasai [1], an HW108A, has a indium antinomide (InSb) sensor [2] which is more effective that silicon due to its high carrier mobility but the package does not contain a preamplifier. Because of its small size, see Figure 2, the Asahi Kasai seems to be more suitable for the manufacture of an array by using off-the-shelf components. Results for the HW-108A will be given in future
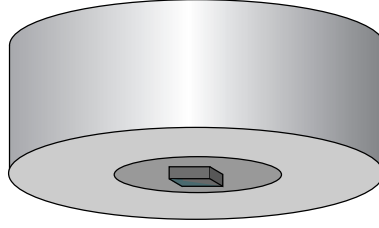
Figure 1: Coil and axially mounted magnetic field sensors.
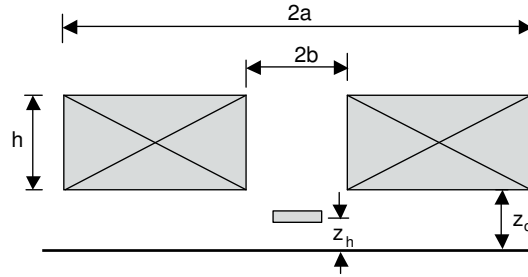
Figure 2: Probe cross section showing key probe parameters.

reports. Here we focus on the measurements taken with the Honeywell device, which has been in production for since the mid eighties and, incidently, is used in the probes for the Nortec Eddyscan.

TABLE 1. Probe Parameters

Probe	P1	P2
Coil O/D $2a$ (mm)	23.34	28.29
Coil I/D $2b$ (mm)	7.86	12.6
Axial length h (mm)	5.0	5.0
Number of turns N	1760	1750
Coil lift-off z_c (mm)	0.55	0.55
Resistance (Ohms)	128.1	166.7
Hall sensor type	HW-108A	634SS2
Manufacturer	Asahi Kasai	Honeywell
Sensor width (mm)	1.3	5.3
Sensor length(mm)	2.1	5.3
Sensor lift-off z_H (mm)	0.1	0.1

Hall sensors are used here for probe validation for several reasons, the two main ones being that the sensor is linear and the region of sensitivity can be can be precisely located at the Hall slice. In a GMR for instance, the sensitive region extends to the flux concentrator to an extent that is difficult to quantify.

Precise ac signal measurements are often plagued by spurious inductive pick-up but in the case of the Asahi Kasai sensor, the bias current to the Hall sensor can be reversed thus inverting the phase of the Hall signal whereas inductive pick-up will retain the same phase following the bias reversal. By subtracting the signals measured with forward and reverse

Figure 3: Asahi Kasai magnetic field sensor. Dimensions are given in millimeters.

sensor current, the result is largely independent of inductive pick-up signals.

1.2.1 Calibration Test

Two precision probes, whose parameters are given in Table 1, have been made and characterized following a procedure given i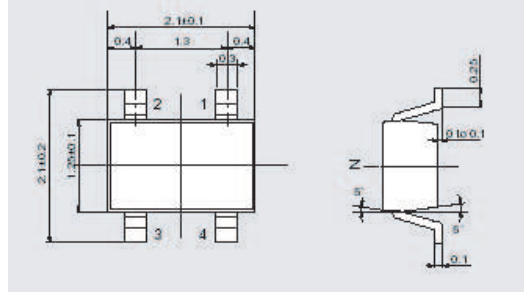n Appendix A. The characterization ensures that the probe performance is in accordance with the assumptions of the simulation and that the sensors is calibrated.

In the characterization procedure, a test is carried out to ensures that the value adopted for the coil probe liftoff yields predictions of coil impedance and its variation with frequency that are consistent with measurements made with the probe on a homogeneous copper slab (See Appendix A for these results). An additional test is performed to ensures that the value adopted for the Hall probe liftoff yields theoretical predictions of the magnetic field variation with frequency at the sensor site that are consistent with experimental field measurements for a probe on the same unflawed copper slab.

In this latter test, the axial magnetic field at the sensor has been predicted for a probe on a copper half-space and compared with calibrated measurements made with the probe an a thick copper plate. One assumes that, because the theory is fairly basic, the theoretical predictions are correct. Then the experimental data is examined to see if the calibration is accurate and the measurement system is functioning correctly without introducing spurious effects. The results of this comparison, Figure 4, show that the experimental field measurements and predictions agree to with 4% over the operating frequency range of the probe.

1.2.2 Square recess

The basic test case for the determination of material loss is a square recess in the bottom surface of a aluminum plate. A comparison between theory and experiment for this case was carried out in Phase I and gave reasonable results. However there was a tendency for the model to overestimate the magnitude experimental field measurements. With the aim of seeking improved agreement between theory and experiment, new data was obtained on the square recess specimen using a new probe and an improved calibration procedure. In addition, the analysis of the field predictions was reviewed and modified.

The recess is 25.45 mm square in the lower face a test piece 4.85 mm thick. The recess was 3 mm deep which means that the material loss is detected through 1.85 mm of aluminum. Phase and amplitude measurements of the magnetic field at the site of the
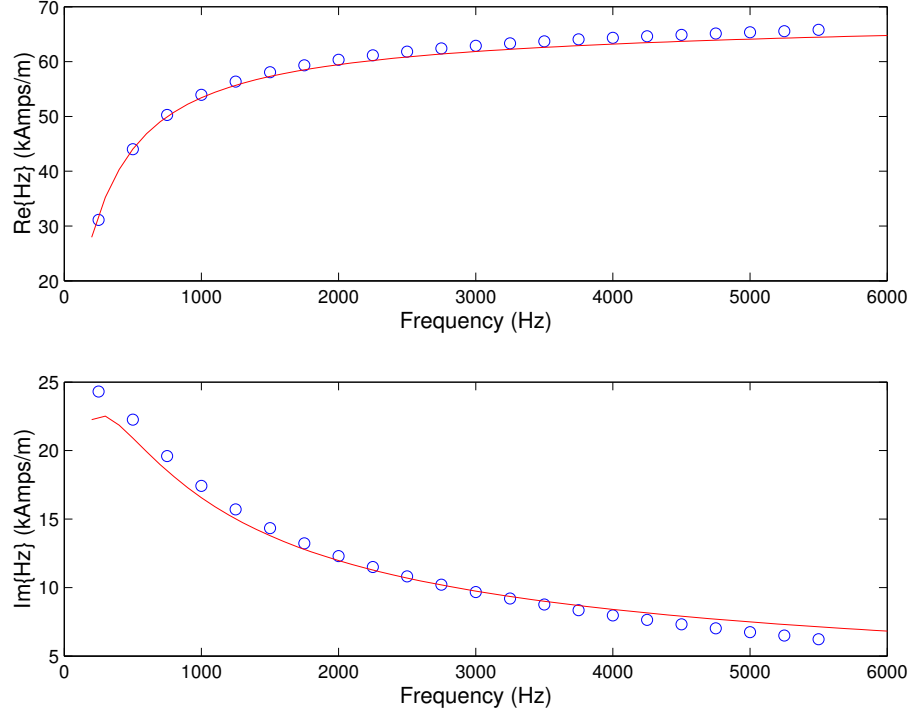
Figure 4: Variation of Hall probe field measurement with the probe on a uniform (i.e. unflawed) copper plate as a function of frequency, comparison of measurements, (circles) with theory, (solid line).

axial sensor were carried out at 2500 Hz. The predicted amplitude and phase of the signal as a function of position for probe P3 (Table 1) is shown in Figure 5 together with the measurements. Note that the noise in the signal is hardly discernable on the graphs.

The predictions are somewhat dependent on the number of volume cells used, although, with a sufficient number the results is stable. With a 12x12x1 array of volume elements the simulation code, taking 5 minutes to run on a 1.5GHz PC, is in good agreement with experiment both for the amplitude and the phase data. The over-prediction error in the amplitude has been reduced by improving the calculation and the calibration precision. However, in view of the accuracy of the prediction on an unflawed plate, which is within 4%, we aim in the future to reduce the discrepancy for flaws to around 5%.

The phase discrepancy for the recess calculation is about 10 degrees. This is not unreasonable in view of the fact the phase can change markedly with the depth of the subsurface flaw or with frequency, as shown in Figure 6. However an effort will be made in the future to reduce the phase discrepancy further.

1.2.3 Holes and fasteners

One of the aims of the current project is to predict signals due to structural features such as holes, fasteners and lap joints and then perform calculations involving these features in the presence of material loss due to corrosion. Work on the combined problem has not yet been completed but experiments on holes, fasteners and lap joints have been performed.

Experimental measurements of the magnetic field due to circular holes in an aluminum
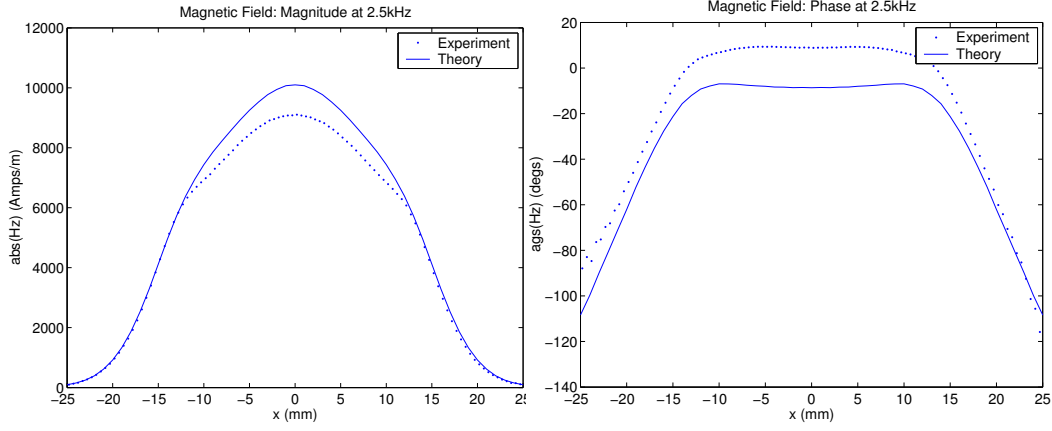
Figure 5: Magnetic field measurements of the signals due to a square recess at a frequency of 2.5kHz using probe P3.

plate, 4.8 mm thick, is shown in Figure 7. These measurements will be compared with theoretical predictions in the future. They were made in order create a stepping stone towards the problem of computing and validating the response for a fastener in a plate, Figure 8. However, time permitted an examination of the field predictions for a fastener only, Figure 8.

The calculations were performed by defining a region whose conductivity differed from that of the host aluminum plate. Because it proved difficult to measure the conductivity of the fastener, results were calculated using a number of different fastener conductivities and the best results chosen, Figure 9. This provides a test of the predicted shape rather than magnitude since the latter was adjust through changes of fastener conductivity to give the best fit.

1.2.4 Lap joint

A basic lap joint structure, Figure 10 was used to simulate the P3 probe signal at 500Hz and 2500 Hz as shown in Figure 11. These results show firstly that the signal has a strong frequency dependance and secondly that the higher frequency signal gives a sharper edge response and therefore may be said to provide a better resolution of the underlying structure.

A comparison between theoretical predictions of the simulation and measurements is shown in Figure 12. The magnitude of the predictions are within about 15% of the measurements. There is a small but significant phase error and some detailed features of the measurements do not appear in the theoretical predictions. This may be due to the fact, common to almost all numerical models at this time, that sharp edges give rise to edge singularities and these are not properly accounted for in discrete representation of the field used for computation.
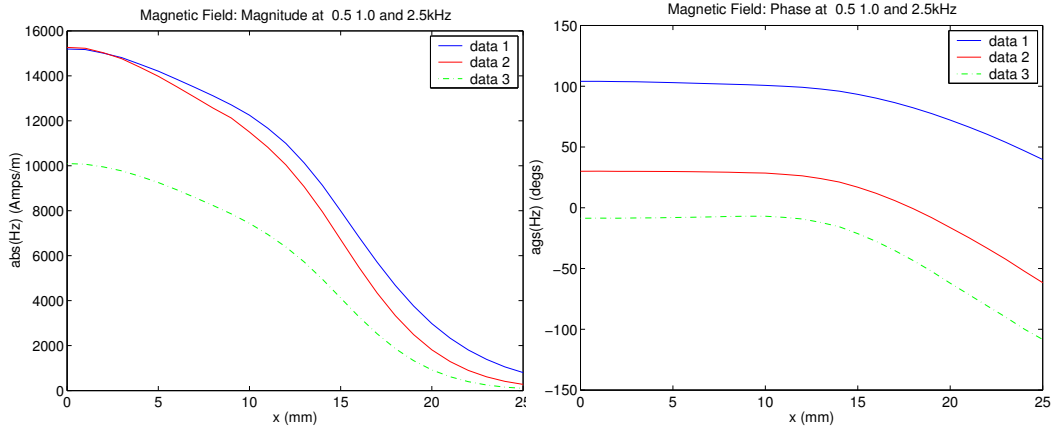
Figure 6: Theoretical predictions of the variation of magnetic field measurements due to a square recess measurements at a frequencies 0.5kHz (data 1) 1.5kHz (data 2) and 2.5 kHz (data 3). Note that the phase of the response changes by over 100 degrees for a frequency change from 0.5kHz to 2.5kHz.

1.3   Conclusions

- **Progress:** It was our intention, at the start of the current project, to validate fully a new volume element code based on a discrete representation of the electromagnetic field in terms of edge elements. This as not been possible firstly because the original plan was perhaps a little ambitious. In our optimism it was felt that a new volume element formulation could be developed and coded within a few months. Other factors included the delays in finalizing the contractual arrangements between ISU and Cassino which lead to delays in completion of the formulation thus limiting the development time that could be spent on the new code. At this stage, the edge element formulation has been coded for a half-space conductor rather than a layered conductor, therefore it need further work before calculations can be compared with measurements on flaws in plates. However selected comparisons between theory and experiment have been carried out using the earlier code based on a traditional volume element scheme.

- **Sensors:** Experiments have been performed with a single sensor probe to test theoretical results and to refine experimental techniques. Two precision made probes with Hall sensors have been built to perform the measurements although in fact, all the experimental data presented here is for a probe with a Honeywell 634SS2 sensor. The Honeywell was first choice simply because it is familiar to us. However the Asahi Kasia HW-108A has a good specification on paper, has the advantage of being enclosed in a small package and therefore seems suitable for a high density array. A single line of such sensors could be mounted less than 2.5 mm apart. By using say three parallel lines of sensor in a staggered array, it would be possible to get measurements in the direction of the senor lines with a separation of about than 1 mm.
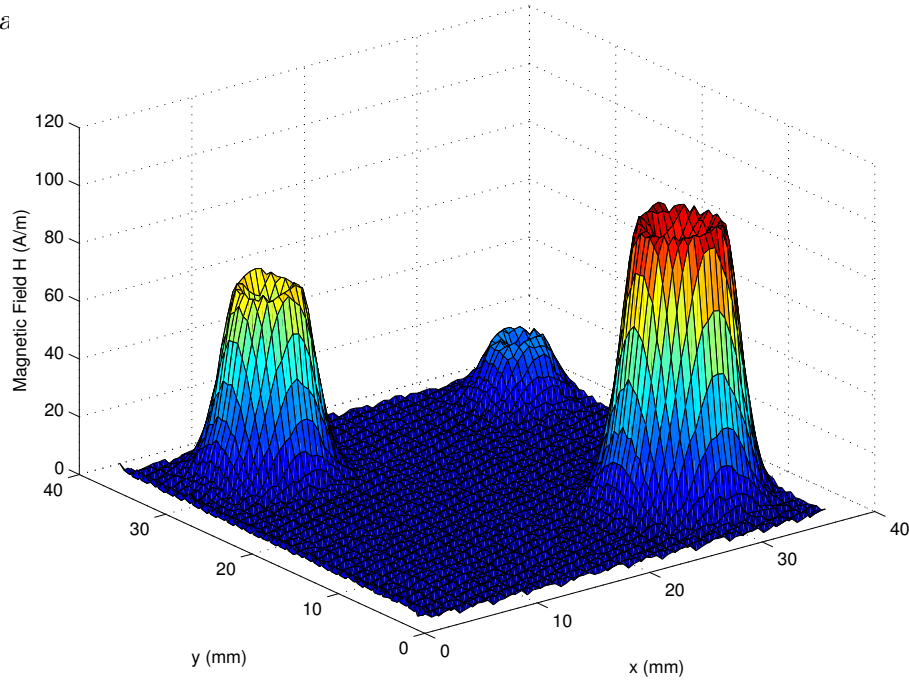
Figure 7: Magnetic field measurements of holes in a conducting plate.

- **Comparisons:** The experimental technique has been greatly improved during this phase of the project and there is no doubt that the data is calibrated correctly and is reliable. Overall the comparison between theory and experiment are reasonable and usually within 10%. The discrepancies are thought to be related to limitations of the model rather than errors in the experiment. It is to be hope that the edge element model will provide further improvements in the accuracy of the predictions.

- **Imaging:** While awaiting the completion of the new formulation by colleagues at the University of Cassino, the question of producing quantitative images of a corrode region was address. This topic is taken up in the following article. At the time of writing, no numerical experiment have not been perform to illustrate the use of the imaging technique but given the simplicity of the approach, this will not be difficult and should be carried out in the near future.
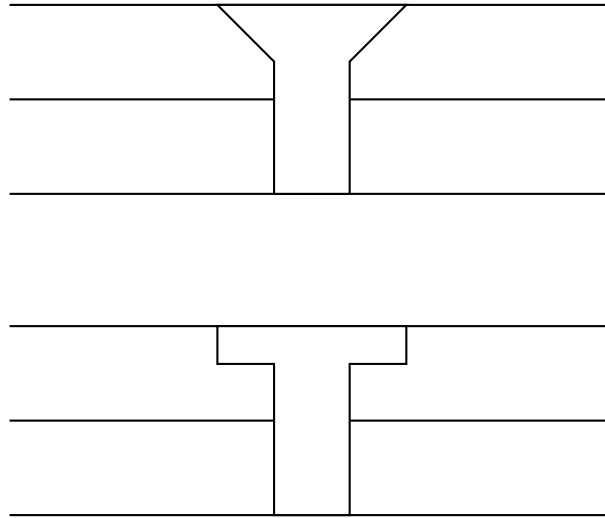
Figure 8: Model representation of a 5.5 mm diameter countersunk rivet in a conducting plate.
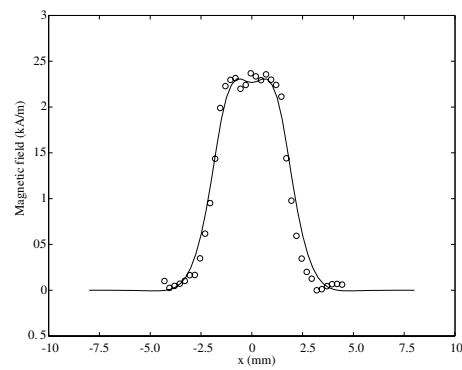
Figure 9: Magnetic field measurements of a 5.5 mm diameter rivet in a conducting plate, comparison of experiment with theory. The unknown fastener conductivity was varied for the best fit.
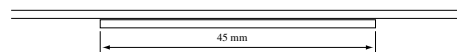
Figure 10: Simplified lap joint: 2mm thick plates, 45 mm wide lap joint with a 0.14 mm insulating layer between.
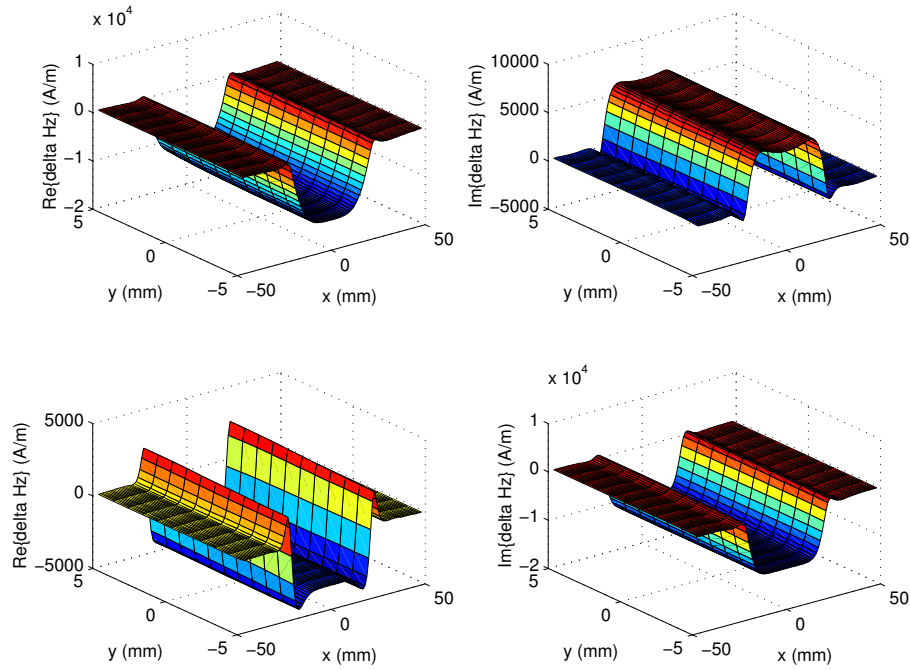
Figure 11: Magnetic field predictions for a simplified lap joint 45 mm wide forming a 2 plate stack with a 0.14 mm gap between plates. The in-phase (real part) and quadrature component (imaginary part) of the field at the axial sensor are shown as a function of position. The upper pair of results are for a frequency of 500Hz and the lower pair for a frequencies of 2.5 kHz.
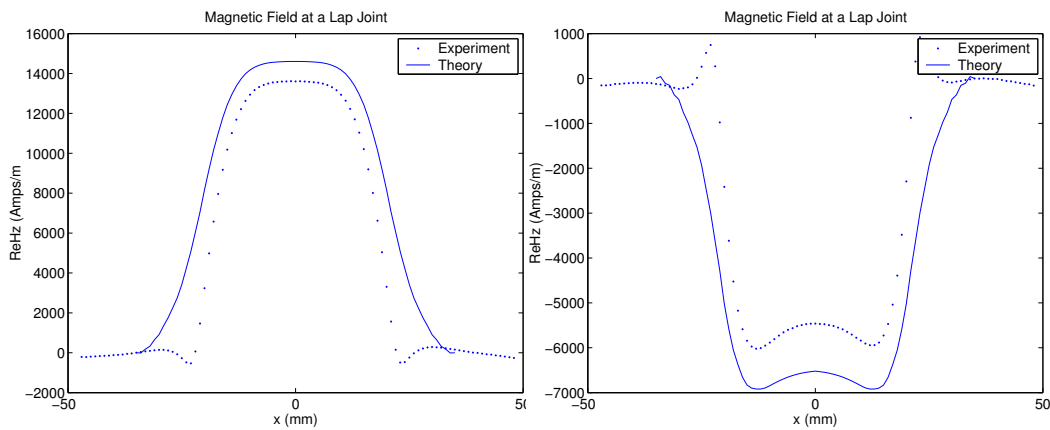
Figure 12: Comparison of the predicted and measured axial magnetic field variation with probe position above a lap joint. The field component in phase with the coil current and in quadrature with the coil current are shown. These are, the real and imaginary parts respectively of the phasor representing the magnetic field.

Bibliography

[1] http://www.asahi-kasei.co.jp/ake/en/ms/hw.htm

[2] http://www.asahi-kasei.co.jp/ake/en/ms/pdf/hw108a.pdf

[3] C. V. Dodd and W. E. Deeds. *J. Appl. Phys.* **39** No.6:2829 (1968).

Appendix A
Probe Characterization and Calibration Procedure

1. **Coil winding:** The coil former dimensions are measured, the coil is wound evenly on the former, the number of turns noted and the outer diameter measured.

2. **Free space impedance:** The coil impedance is measured in free space as a function of frequency over the operating frequency range of the probe (40 Hz-10,000 Hz in this case) using an impedance analyzer (Agilent 4294A). The free space self inductance of the probe, L_0 in the zero frequency limit is found by extrapolating the self-inductance data to the zero frequency limit. The theoretic value of L_0 is compared with the experimental value to check that it is consistent with the coil dimensions and the number of turns. If the calculated L_0 disagrees with measurement, the outer radius of the coil is incrementally adjusted, Figure A1 until agreement is reached.

3. **Correction inter winding capacitance** The effective shunt capacitance of the coil, C_0 is found. This value is used to correct measured impedance before comparison with theory.

4. **Half-space coil impedance:** The coil impedance is measured as a function of frequency with the probe on a thick conducting copper plate. Measurements are made over the operating frequency range of the probe. These measurements are then corrected for the effect of the shunt capacitance and compared with the theoretical predictions from the theory of Dodd and Deeds[3]. A root mean square error function is used to quantifying the fit of all the data to the theory and is calculated from

$$\mathcal{E}^2 = \sum_{m=1,M} |Z_m^{(\text{expt})} - Z(\omega_m)|^2 \tag{A1}$$

where $Z_m^{(\text{expt})}$ is the corrected experimental measurement at frequency ω_m, $Z(\omega_m)$ is the theoretical value and the sum is over for all M measurements. The effective coil lift-off value z_c is then adjusted until this error is a minimum.

5. **Sensor location:** The Hall sensor is then mounted on the coil axis and the location of the sensitive region found from a micro-focus X-ray.

6. **Magnetic sensor calibration:** The Hall sensor is calibrated in air as follows. A standard resistor is connected in series with the coil and the ac signal output from a Stanford lock-in analyzer applied across the coil and resistor. The lock-in is used to determine the coil current and the Hall voltage. Because the coil is in air, a simple expression can be used to determine the magnetic field at the site of the Hall sensor. Since the field is known, the sensor can be calibrated over the operating frequency range of the probe.

7. **Half-space field measurements:** The field measured by the Hall device is then determine as a function of frequency with the probe on a thick metal copper plate of known conductivity. These results are then compared with the theoretical values and a least squares error function computed as for the impedance data:

$$\mathcal{F}^2 = \sum_{m=1,M} |H_m^{(\text{expt})} - H(\omega_m)|^2 \tag{A2}$$

The Hall device liftoff value, z_H, is them varied until this error function reaches a minimum.
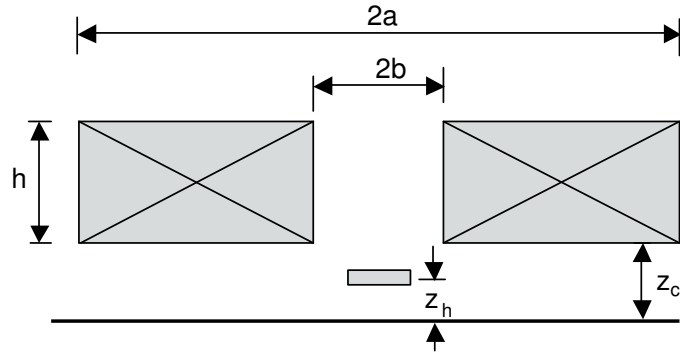
FIGURE A1. Probe cross section showing key probe parameters.

Appendix B
Probe Characterization and Calibration Results

Results given in this appendix refer to the characterization and calibration of probe P3 (see Table 1 or the main text for its nominal dimensions) following the procedure given in Appendix A.

B1   Coil characterization

Having wound the coil for probe P3, the impedance was measured in air as a function of frequency, Figure B1. The coil resistance varies little with frequency, although at high frequency it increases due to the skin effect in the windings.

Typically the predicted self inductance of the probe calculated from the measured dimensions is less the experimental value. This is attributed to the fact that direct measurement of the outer diameter overestimates the effective value due to unevenness in the windings. A reduced value of the outer diameter is adopted for which the predicted self-inductance matches the measured value in the low frequency limit, found by extrapolation of the measurements to zero frequency. The low frequency limiting value of the self-inductances is 0.054634 mH and the adjusted outer radius is 13.518 mm.

Table B1: Coil Parameters

Parameter	Value	Notes
Inner radius	6.300 mm	Measured
Outer diameter	13.518 mm	Fit of self inductance predictions
Number of turns	1750	Counted
Height	4.860 mm	Measured
Liftoff	0.710 mm	Fit of half-space impedance predictions

Next, multi-frequency impedance data were obtained for the probe on a thick copper plate. Before these data can be used for comparison with theory, a correction must be made for the effects of parallel capacitance in the probe cable and between the windings. The Dodd and Deeds [3] model does not account for the effects of stray capacitance and so simple circuit theory is used in a compensation scheme.

The experimental impedance change due to a thick copper plate is compared with Dodd and Deeds predictions [3] of the impedance change due to a copper half-space conductor. The coil lift-off, the distance between the base of the coil and the surface of the conductor, is adjusted for best agreement. Matching with Dodd and Deeds predictions seems to be the most accurate method of estimating the coil lift-off, direct measurement being difficult. In this case a value of 0.71 mm was determined by impedance fitting. See Figures B2 for the comparison between theory and experiment for the coil impedance on a copper half-space. The coil parameters found following the impedance measurements are summarized in Table B1.
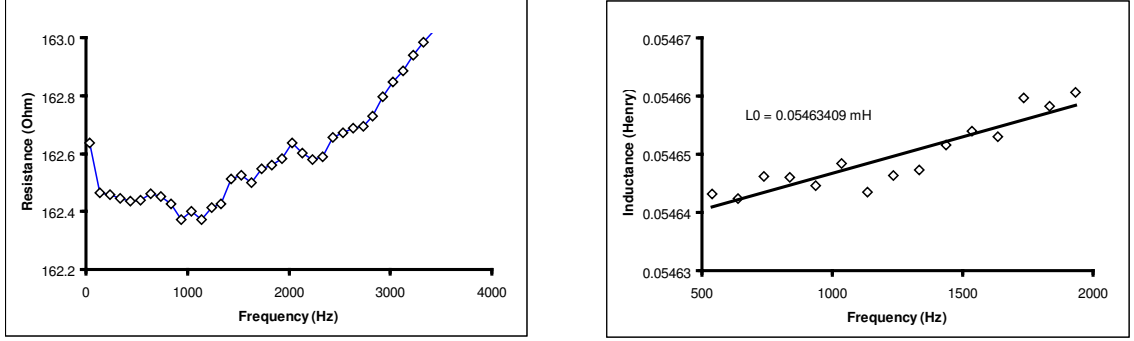
Figure B1: Coil resistance and self-inductance variation with frequency.

B2 Sensor Calibration

The coil current excitation is provided by a lock-in amplifier output and measured using the lock-in by monitoring the voltage drop across a $10\,\Omega$ standard resistor in series with the coil. Similarly the Hall sensor voltage is measured by the lock in. Because the instrument acts as a voltage source and the load is inductive, the load impedance and the coil current varies with frequency and hence the Hall signal varies with frequency as shown by probe measurements in free space, Figure B3.

The ratio of the Hall voltage to the coil current should be reasonably constant provided that the operating frequency range is within the bandwidth of the Hall sensor preamplifier. This is certainly true for the dominant real part[1], Figure B4. It is estimated that the Hall sensor, like the coil, has a lift-off of 0.71 mm. Using this value and the other probe parameters, the field on the coil axis at the site of the sensor has been calculated. The calculated value of the field at the sensor for the probe in free space per unit coil current is $H_0 = 81,316$Amps/m. Note also the characteristic parameter $R_{HC} = 5.317\Omega$ which is the real part of the ratio of the Hall voltage to the probe current with the probe in air. This value varies slightly, see Figure B4, but we adopt a constant value determined at 2000 Hz. From measurements of the Hall sensor voltage V_H and the coil current I_c, the magnetic field at the sensor is given by

$$Hz = \frac{H_0}{R_{HC}}\frac{V_H}{I_c} \tag{B1}$$

Using this calibration procedure, the axial magnetic field at the sensor has been predicted for a probe on a copper half-space and compared with calibrated measurements made with the probe on a thick copper plate. These results are show in the main text.

---

[1]The real part corresponds to the component in phase with the reference signal of the lock-in.
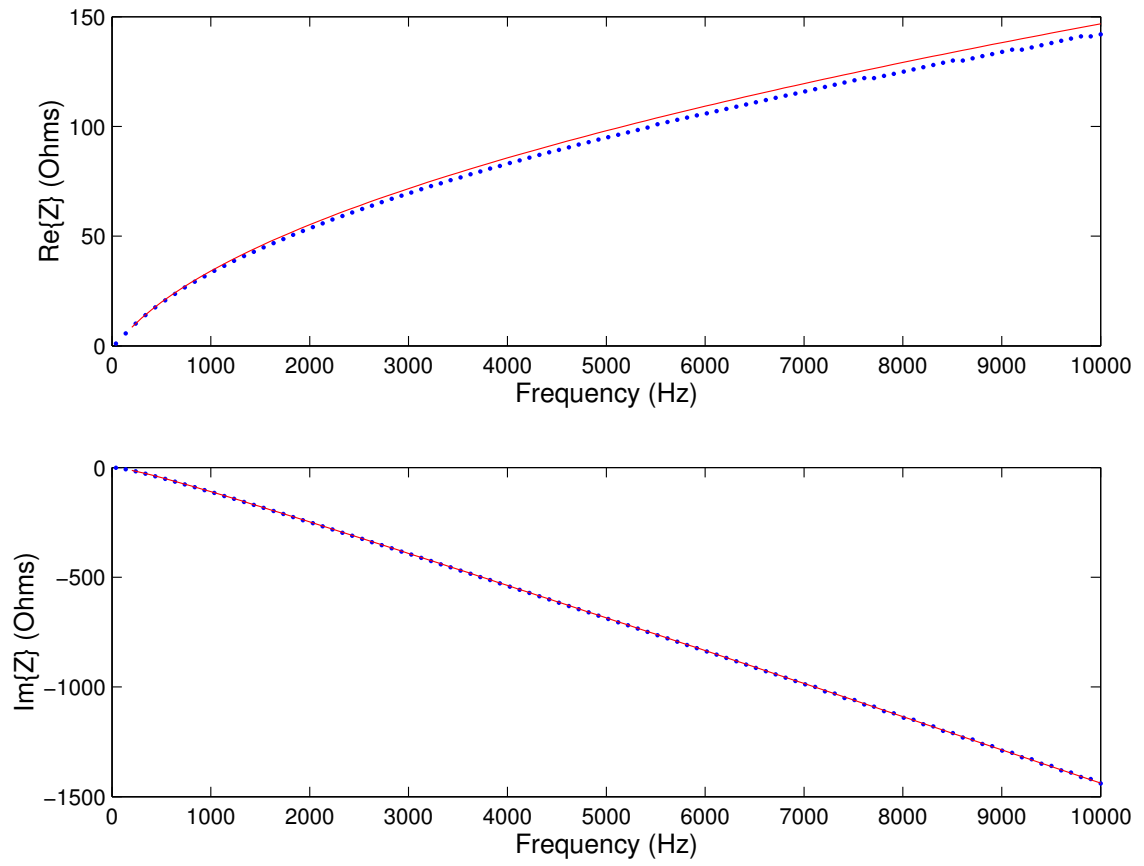
Figure B2: Coil impedance variation with frequency; comparison of experiment, circles, with theory, line.
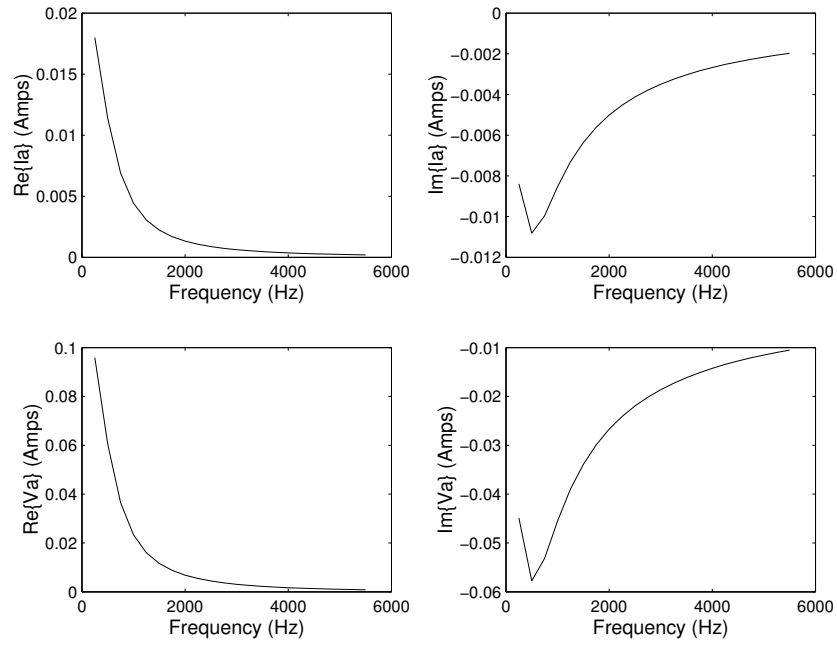
Figure B3: Coil current I_a and magnetic field sensor voltage V_a variation with frequency in free space.

Figure B4: The ratio of sensor voltage V_a to coil current I_a as a function of frequency for the probe in free space.

Article 2

Imaging and Inversion of Corrosion Loss

2.3 Estimations of Material Loss

In eddy current NDE, scan data is often presented in the form of a false color map or an 'image'. Typically the data is color coded with minimal pre-processing and because measurements contain phase as well as amplitude information some of this information is necessari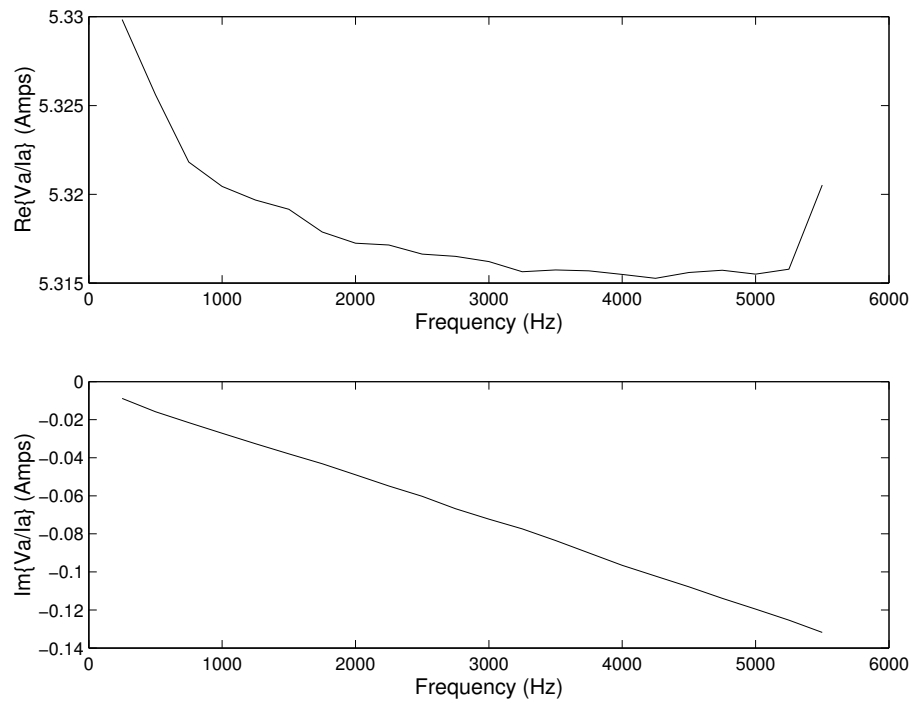ly lost when creating the image. Ideally one would like a map of the material loss rather than a simple probe dependent data image but this seems to require a complicated and time consuming inversion algorithm which would extract quantitative material loss data from sensor signals (such a scheme, incidently, has not yet been implemented even though the methods needed to accomplish the task are known [1]).

Image processing techniques using Fourier transformations and filtering are fast, simple and can reduce the noise but seem better suited to the important but somewhat cosmetic task of improving the appearance of the image rather than extracting quantitative estimates of material loss. Can we get a contour or false color map of the material loss via a method that is fast, like the standard image processing methods and avoids the computational burden of a full blown inversion? For small amounts of material loss in a flat plate, the answer appears to be "Yes".

2.3.1 Eddy current imaging

Material loss in the form of an overall plate thinning can be estimated by elementary calibration techniques. One simply carries out measurements of the eddy current signal for a number of different plate thickness and records the relationship between signal and plate thickness, possibly in the look-up table. This is a very limited way of estimating material loss for a number of reasons. For example, it cannot deal with local variations of thickness and gives no indication of the surface roughness. In addition, it will not work were a signal due to a structural feature interferes with the material loss signal.

The last of these problems is difficult to overcome and will not be addressed here but the other two can be dealt with using a relatively simple method based a deconvolution of the probe and flaw functions. For a flat plate, or for a stack of flat plates, with local thinning in one plate due to say corrosion, the flaw signal can be expressed as a convolution of a flaw and a probe function having the form

$$V(x, y) = \int_{-\infty}^{\infty} \int_{-\infty}^{\infty} H(x - x', y - y') F(x', y') \, dx' \, dy', \tag{2.2}$$

where V represents the measured signal, H is the point spread function of the probe and F the flaw function. This expression is valid if the material loss is small compared with the plate thickness (say less than 15%). Equation (2.2), may be written as

$$V = H * F \tag{2.3}$$

where the $*$ represents a two dimensional convolution. The deconvolution can be carried out to find the flaw function using Fourier transform techniques and the Weiner filter. Thus, an approximation of the deconvolved function is obtained from the inverse 2-D Fourier transform of

$$\widetilde{F} = \frac{\widetilde{H}^*}{\widetilde{H}\widetilde{H}^* + K}\widetilde{V} \tag{2.4}$$

where $\widetilde{F}$ is the 2-D Fourier transform of the flaw function, $\widetilde{F}$ is the 2-D Fourier transform of the point spread function and K is a constant depending on the noise in the data. Equation (2.2) is justified later in this article but first, it is helpful to recall its previous use in eddy current signal processing.

2.3.2 Surface crack imaging

The idea of expressing an eddy current probe signal as a convolution is not new. An early attempt to deconvolve eddy current signals due to surface defects such as cracks in turbine disks was made by Joyson, McCary, Oliver Silverstein-Hedengren and Thumhart [2] at GE's Corporate Research and Development. Clearly, the work at GE and elsewhere which treats eddy current images as convolutions, would have a better foundation if it could be justified theoretically for surface cracks. Equation (2.2) is simply assumed, as a working hypothesis, in the hope that the results justify the approach *á posterior* but the physics of the problem seems at variance with the assumption.

The interaction with a crack depends on the direction of the induced current which must be taken into account even if the formula used for the measured signal, equation (2.2), is a scalar formula. In the GE work, a tape head probe was used to control the field direction giving a flaw image which is dependent on the probe orientation. There are disadvantages in being restricted to tape head probes and having to deal with crack images that are orientation dependent. However, the probe response to subsurface corrosion is not strongly direction dependent, which suggests that deconvolution in this context may successful for a wide range of probes.

A time-harmonic field is typically represented by a phasor, hence the interaction with a surface crack is described by a complex vector process in three dimensions. It is not clear how the crack signal would reduce theoretically to a real scalar convolution in two dimensions as represented by (2.2). However, the theoretical reduction to a complex 2D scalar convolution can be performed for limited subsurface corrosion loss in a plate.

2.3.3 Imaging subsurface corrosion in a plate

Although (2.2) has not been justified theoretically for surface flaws such as cracks, it can be supported for small amounts of material loss in plates. The reason for this is that plate thinning gives a small perturbation of the field over a relatively large region whereas a crack gives a large localized field perturbation.

In general the flaw signal detected by a driver pick-up probe can be derived rigorously from a reciprocity principle [3] to give, suppressing the probe coordinates,

$$V_{12} = -\int_{\Omega_0} \mathbf{E}^{(1)}(\mathbf{r}') \cdot \mathbf{P}(\mathbf{r}')\, d\mathbf{r}' \tag{2.5}$$

for unit coil current, where Ω_0 is the flaw region, $\mathbf{E}^{(1)}(\mathbf{r}')$ is the unperturb field at the flaw due to the pick-up sensor[2] and $\mathbf{P}(\mathbf{r})$ is the current dipole density of the flaw induced

---

[2]If the pick-up happens to be a magnetic field sensor then the corresponding electric field is that produced by a magnetic dipole at the site of the sensor.

by the driver. A plate or a system of parallel plates perpendicular to the z-axis has a translational invariance which allowing the unperturbed electric field to be written as $\mathbf{E}^{(n)}(x - x', y - y', z')$ with x and y as the probe coordinates. For pick-up and driver, $n = 1, 2$ respectively.

For small amount of material loss due to corrosion at the surface of a plate, the integration over the direction normal to the surface of the unflawed plate, the $z-$direction in this case, can be approximated as

$$\int \mathbf{E}^{(0)}(\mathbf{r}') \cdot \mathbf{P}(\mathbf{r}') \, dz' = \sigma_0 \mathbf{E}^{(1)}(x - x', y - y', z_0) \cdot \mathbf{E}^{(2)}(x - x', y - y', z_0) \delta z(x', y') \quad (2.6)$$

where $\delta z(x', y')$ is the height of the loss region, z_0 is the $z-$coordinate of the the original (unflawed) surface and $\mathbf{E}^{(2)}(x', y', z_0)$ is the unperturbed field due to the driver coil. This approximation can be justified by using the approach described in reference [1] where an expression for the variation of the probe response is given for a small variation in the location of a conducting surface. The variation $\delta z(x', y')$ is interpreted as being associated with material loss due to corrosion and the variation of probe signal, written as V_{12}, represents the signal due to material loss.

Substituting (2.6) into (2.5) and putting

$$H_{12}(x - x', y - y') = -\sigma_0 \mathbf{E}^{(1)}(x - x', y - y', z_0) \cdot \mathbf{E}^{(2)}(x - x', y - y', z_0) \quad (2.7)$$

gives

$$V_{12}(x, y) = \int_{-\infty}^{\infty} \int_{-\infty}^{\infty} H(x - x', y - y') \delta z(x', y') \, dx' \, dy' \quad (2.8)$$

which is a two dimensional convolution for the material loss $\delta z(x, y)$.

2.4   Conclusion

The thesis presented here is that the deconvolution via Weiner filtering applied to eddy current data images of surface cracks has not been justified theoretically and is not effective. However, the same procedure can be used to find the material loss from a flat plate in a stack of flat plates. The basic requirement is that the loss estimator $\delta z(x, y)$, must be small compared to the plate thickness.

A key practical question for further consideration is one of resolution. It is well known that corrosion can be intensely localize in the form of pits which may be small. The ability to find the depth of such features using the Fast Fourier Transform methods may be limited because of both the fundamental limitation of the eddy current modality, it is after all a highly diffusive phenomena, and in addition there are sampling limits which reduce resolution. The former can be mitigated by using higher frequencies, the latter by using a high density sensor array.

Bibliography

[1] S. J. Norton, J. R. Bowler, *J. Appl. Phys.* **72(2)**, 501-512 (1993).

[2] R. E. Joyson, R. O. McCary, D. W. Oliver, K. H. Silverstein-Hedigren and L. L. Thumhart, IEEE Trans. Mag. Vol Mag-22, No. 5 pp1260-1262, 1986.

[3] R. F. Harrington, *Time Harmonic Electromagnetic Fields* (New York, McGraw-Hill 1961).

Article 3

Eddy current excitation using a racetrack coil with a sensor array for magnetic field measurement

J. R. Bowler and V. Katyal

Iowa State University, Center Nondestructive Evaluation,
ASC II, 1915 Scholl Road, Ames Iowa 50011.

Abstract Calculations have been performed to determine the response of a new eddy current probe for the detection of subsurface flaws in planar multilayered structures. The probe consists of a racetrack coil and a linear array of solid state sensors for detecting perturbations in the electromagnetic field due to defects. The sensor array allows field measurements to be made at a number of closely spaced locations without moving the probe and thereby accelerates the inspection process. A magnetic shell model of the probe is used for finding the electric field in the unflawed structure. The fields due to the linear "straights" and the semicircular "bends" are found separately and added to give the combined field of the racetrack coil. The flaw response is then computed using a volume element calculation. In order to validate the calculation, field predictions for a racetrack coil having straights of zero length are compared with results for a circular coil. The results are found to be consistent.

3.1   Introduction

In eddy current inspection, an induction coil is often used both to induce current in a conducting component and to detect magnetic field perturbations due to flaws. For subsurface defects, a low frequency excitation ensures an adequate depth of field penetration. However, at lower frequencies the effectiveness of the coil as both inducer and sensor is diminished since electromagnetic induction depends on the rate of change of magnetic flux. To overcome the limitations of the induction coil as a low frequency field sensor, a solid state device, such as a giant magneto-resistor or Hall sensor, can be used instead. A coil used only as driver can be larger than otherwise without compromising the spatial resolution of the measurements. The large coil can produce a greater field while good spatial resolution is obtained by using small sensors.

This article gives the analysis of an eddy current probe for the detection of subsurface flaws in multilayered structures such as aircraft skins. The probe contains a racetrack coil with semi-circular bends and linear straights, Fig. 1. The magnetic field between the straights is measured using a linear array of magnetic field sensors. The sensor array samples the magnetic field at multiple sites without moving the probe and hence reduces the inspection time. The overall objective of this work is to evaluate the capabilities of array probes and assess their performance for the detection of cracks, material loss and surface roughness due to corrosion. Here we focus on the details of the coil field calculation.

The theory for computing the electromagnetic field of a racetrack coil, Fig. 1, has been developed by determining separately the electric field due to the bends and the straights

and summing to obtain the total field. Section II gives the theory for the straight linear coil elements and Section III describes the solution for the D-coil representing a semicircular bend. The results and conclusions follow the analysis sections.

3.2 Linear Coil Field

The following account describes the calculation of the electric field induced in a conductor by a time-harmonic current in a linear coil consisting of only the straight parts of the racetrack coil shown in Fig. 1. The current path is closed by joining the ends of the straights by current filaments but ultimately the effect of these filaments is cancelled by similar filaments added to the representation of the bends. Results are given for a field in a homogeneous half-space conductor in the region $z < 0$, and an infinite conducting plate. However, similar results for layered conductors are readily obtained by simply changing the Green's functions used in the present calculation in favor of one which embodies the correct interface conditions of a stratified conductor. The magnetic dipole formulation used in this section to represent the field of the straights is also used for the bends in the next section.

Consider a non-magnetic conductor occupying the half-space defined by $z < 0$, excited by a current source. The electric field in adjoining half-spaces is a solenoidal solution of,

$$\nabla^2 \mathbf{E}(\mathbf{r}) = \jmath\omega\mu_0\,\mathbf{J}(\mathbf{r}),\ \ z \geq 0 \qquad \text{and} \qquad \left(\nabla^2 - \jmath\omega\mu_0\sigma\right)\mathbf{E}(\mathbf{r}) = 0, \qquad z < 0, \qquad (3.1)$$

where σ is the conductivity of the conductor. The electric field, being transverse to the $z-$direction and having zero divergence, can be expressed in terms of a transverse electric (TE), scalar potential:

$$\mathbf{E}(\mathbf{r}) = -\jmath\omega\mu_0\nabla \times \hat{z}\psi'(\mathbf{r}), \qquad (3.2)$$

where $\hat{z}$ is a unit vector in the preferred direction. The transverse source current $\mathbf{J}(\mathbf{r})$, having zero divergence, can similarly be written in transverse scalar form as

$$\mathbf{J}(\mathbf{r}) = \frac{1}{\mu_0}\nabla \times [\hat{z}M(\mathbf{r})]. \qquad (3.3)$$

The function $M(\mathbf{r})$ represents the current source in terms of the magnetic dipole density, the orientation of the polarization being in the $z-$direction. This is an adaptation of the magnetic shell model which represents a filamentary current loop in terms of magnetic shell bounded by the loop. Here, the magnetic dipole distribution occupies a volumetric region between the upper and lower extent of the coil where $h + c \geq z \geq h - c$, $2c$ being the height of the coil and h the height of the mid point of the coil above the surface of the conductor.

Equations (3.2) and (3.3) are substituted into (3.1) to give

$$\nabla^2\psi'(\mathbf{r}) = -\frac{1}{\mu_0}M(\mathbf{r}),\ \ z \geq 0 \qquad \text{and} \qquad \left(\nabla^2 - \jmath\omega\mu_0\sigma\right)\psi'(\mathbf{r}) = 0,\ \ z < 0. \qquad (3.4)$$

An expression for the solution in terms of a Green's function, satisfying

$$\nabla^2 G(\mathbf{r}, \mathbf{r}') = -\delta(\mathbf{r} - \mathbf{r}'),\ \ z \geq 0 \qquad \text{and} \qquad \left(\nabla^2 - \jmath\omega\mu_0\sigma\right)G(\mathbf{r}, \mathbf{r}') = 0,\ \ z < 0, \qquad (3.5)$$

is written as

$$\psi'(\mathbf{r}) = \frac{1}{\mu_0}\int_{\Omega_0} G(\mathbf{r}, \mathbf{r}')\,M(\mathbf{r}')\,d\mathbf{r}, \qquad (3.6)$$

where the Green's function, like ψ', is continuous at the air conductor interface, has a continuous normal gradient and vanishes at infinity. The Fourier transform with respect to x and y is written

$$\widetilde{f}(u,v) = \int_{-\infty}^{\infty} \int_{-\infty}^{\infty} f(x,y) e^{-iux-ivy} \, dx \, dy. \tag{3.7}$$

Hence by taking the Fourier transform of equation (3.6) with respect to x and y, and noting the convolutional properties of the integral, it is found that

$$\widetilde{\psi}'(u,v,z) = \frac{1}{\mu_0} \int_{h-c}^{h+c} \widetilde{g}(u,v,z,z') \, \widetilde{m}(u,v,z') \, dz', \tag{3.8}$$

where the integration is between the lower and upper limits of the source coil and $\widetilde{g}$ and $\widetilde{m}$ are the Fourier transforms of G and M respectively.

The y-component of the current density in the straight elements of the source coil, Fig. 1, is written as

$$J_y(\mathbf{r}) = \begin{cases} nI \, \text{sign}(x), & h-c \le z \le h+c, \quad b \le |x| \le a, \quad |y| \le d, \\ 0, & \text{otherwise} \end{cases} \tag{3.9}$$

where I is the current, n the number of turns per unit area and the current is deemed to flow in a counter-clockwise direction viewed from above. It can be deduced from (3.3), by writing

$$M(x,y,z) = \begin{cases} \mu_0 nI f(x,y), & h-c \le z \le h+c \\ 0, & \text{otherwise} \end{cases} \tag{3.10}$$

that

$$f(x,y) = \begin{cases} a-b, & 0 \le |x| \le b, \quad |y| \le d, \\ a-|x|, & b \le |x| \le a, \quad |y| \le d, \\ 0, & \text{otherwise.} \end{cases} \tag{3.11}$$

Because $f(x,y)$ is even in x and y, the Fourier transform may be written in the form of the double cosine integral

$$\begin{aligned} \widetilde{f}(u,v) &= 4 \int_0^{\infty} \int_0^{\infty} f(x,y) \cos(ux) \cos(vy) \, dx \, dy \\ &= -\frac{4}{u^2 v} [\cos(ua) - \cos(ub)] \sin(vd). \end{aligned} \tag{3.12}$$

An expression for the electric field which can be evaluated numerically is obtained in the following way. The Fourier transform of (3.2) with respect to x and y is

$$\widetilde{\mathbf{e}}(u,v,z) = -\omega\mu_0(v\hat{x} - u\hat{y}) \, \widetilde{\psi}'(u,v,z) \tag{3.13}$$

where $\widetilde{\psi}'$ is given by (3.8) and (3.10) as

$$\widetilde{\psi}'(u,v,z) = nI \widetilde{f}(u,v) \int_{h-c}^{h+c} \widetilde{g}(u,v,z,z') \, dz', \qquad z < 0. \tag{3.14}$$

For a half-space conductor

$$\widetilde{g}_{\text{H-S}}(\kappa, z, z') = \frac{1}{\gamma + \kappa} e^{\gamma z - \kappa z'} \tag{3.15}$$

where $\gamma = \sqrt{\kappa^2 + j\omega\mu_0\sigma}$, taking the root with a positive real part. Similarly, Green's function for a slab is computed by taking into account the reflection from the internal surfaces,

$$\widetilde{g}_{\text{Slab}}(\kappa, z, z') = \frac{1}{\gamma + \kappa} e^{\gamma z - \kappa z'} \frac{1 + \Gamma e^{-2\gamma(d+z)}}{1 - \Gamma^2 e^{-2\gamma d}} \tag{3.16}$$

where $\Gamma = \frac{\gamma - \kappa}{\gamma + \kappa}$, the reflection term and $d = $ height of the slab. Performing the integration in (3.14) gives

$$\widetilde{\psi}'(u, v, z) = 2nI\,\widetilde{f}(u, v)\,\widetilde{g}(u, v, z, h)\sinh(\kappa c)/\kappa, \qquad z < 0, \tag{3.17}$$

hence by substituting into (3.13) it is found that

$$\widetilde{\mathbf{e}}(u, v, z) = -2\omega\mu_0 nI \frac{v\hat{x} - u\hat{y}}{\kappa}\,\widetilde{f}(u, v)\,\widetilde{g}(u, v, z, h)\sinh(\kappa c), \qquad z < 0. \tag{3.18}$$

The electric field can now be computed using a fast-Fourier-transform algorithm.

3.3 D-Coil Field

Two D-coils are used to represent the bends of the racetrack coil, Fig. 1. Using essentially the same formulation that was used for the linear coil, ψ' for the D-coil is written as in (3.6). It is convenient to express the Green's function in cylindrical polar coordinates, as

$$G(\mathbf{r}, \mathbf{r}') = \frac{1}{2\pi} \sum_{m=0}^{\infty} \epsilon_m \cos[m(\phi - \phi')] \int_0^\infty J_m(\kappa\rho)J_m(\kappa\rho')\,\widetilde{g}(\kappa, z, z')\kappa\,d\kappa, \quad z < 0, \tag{3.19}$$

which can be derived using an approach given by Morse and Feshbach [1]. In (3.19), ϵ_m is the Neumann factor: $\epsilon_0 = 1$ and $\epsilon_m = 2$ $(m = 1, 2, 3, \ldots)$. For the interior of a half-space conductor, $\widetilde{g}$ is given by (3.15). For for a slab, $\widetilde{g}$ is given by (3.16). In order to evaluate (3.6), the explicit form of $M(\mathbf{r})$ appropriate for the D-coil must be found. This form is developed as follows.

The azimuthal counter-clockwise current in a D-coil is written as

$$J_\phi(\mathbf{r}) = \begin{cases} nI, & h - c \le z \le h + c, \qquad 0 \le \phi \le \pi, \qquad b \le \rho \le a \\ 0, & \text{otherwise.} \end{cases} \tag{3.20}$$

where I is the current, n the number of turns per unit area. It can be deduced from (3.20), by writing

$$M(\rho, \phi, z) = \begin{cases} \mu_0 nI f_D(\rho), & h - c \le z \le h + c, \qquad 0 \le \phi \le \pi, \\ 0, & \text{otherwise} \end{cases} \tag{3.21}$$

that

$$f_D(\rho) = \begin{cases} a - b, & 0 \le \rho \le b, \\ a - \rho, & b \le \rho \le a, \\ 0, & \text{otherwise} \end{cases} \tag{3.22}$$

It is now possible to obtain ψ' by substituting equations (3.19) and (3.21) into (3.6). Integration with respect to ρ', ϕ' and z' gives a summation of integrals with respect to κ:

$$
\begin{aligned}
\psi'(\mathbf{r}) \;=\; nI\Bigg[& \frac{1}{\pi} \sum_{\lambda=0}^{\infty} \frac{4}{2\lambda+1} \sin[(2\lambda+1)\phi] \\
& \times \int_0^{\infty} [J_{2\lambda+1}(\kappa\rho)\mathcal{F}_{2\lambda+1}(a,b,\kappa)\,\widetilde{g}\,(\kappa,z,h)\sinh(\kappa c)]\,d\kappa \\
& + \int_0^{\infty} [J_0(\kappa\rho)\mathcal{F}_0(a,b,\kappa)\,\widetilde{g}\,(\kappa,z,h)\sinh(\kappa c)]\,d\kappa \Bigg]
\end{aligned}
\tag{3.23}
$$

where

$$
\begin{aligned}
\mathcal{F}_\nu(a,b,\kappa) \;=\;& \int_0^a f_D(\rho)J_\nu(\kappa\rho)\rho\,d\rho \\
=\;& \frac{1}{\kappa^2}\Big[a\mathcal{J}_\nu^{(1)}(\kappa a) - b\mathcal{J}_\nu^{(1)}(\kappa b) \Big] - \frac{1}{\kappa^3}\Big[\mathcal{J}_\nu^{(2)}(\kappa a) - \mathcal{J}_\nu^{(2)}(\kappa b) \Big]
\end{aligned}
\tag{3.24}
$$

with f_D given by (3.22) and

$$
\mathcal{J}_\nu^n(z) = \int_0^z x^n J_\nu(x)\,dx.
\tag{3.25}
$$

These functions are evaluated for $\nu > 2$ with the aid of a recursion relationship

$$
(\nu - n)\mathcal{J}_{\nu+1}^n(z) = -2\nu z^n J_\nu(z) + (\nu + n)\mathcal{J}_{\nu-1}^n(z)
\tag{3.26}
$$

derived using Eq 11.3.6 of reference [2].

The integrals with respect to κ must be computed numerically and the summation in (3.23) truncated at a suitable order depending on the required accuracy of the result. For the double-D filament loop [3] a truncated series of five terms is sufficiently accurate in most cases and the same is true for the series in (3.23) representing the potential due to a racetrack coil bend.

From equation (3.2), the electric field in cylindrical coordinates is

$$
\mathbf{E}(\mathbf{r}) = -\jmath\,\omega\mu_0 \left(\hat\rho\frac{1}{\rho}\frac{\partial}{\partial\phi} - \hat\phi\frac{\partial}{\partial\rho} \right) \psi'(\mathbf{r}).
\tag{3.27}
$$

The components of the electric field are therefore,

$$
\begin{aligned}
E_\rho(\mathbf{r}) \;=\; & -\frac{4\jmath\,\omega\mu_0 nI}{\pi\rho} \sum_{\lambda=0}^{\infty} \cos[(2\lambda+1)\phi] \\
& \times \int_0^{\infty} J_{2\lambda+1}(\kappa\rho)\mathcal{F}_{2\lambda+1}(a,b,\kappa)\,\widetilde{g}\,(\kappa,z,z_0,h)\sinh(\kappa c)\,d\kappa
\end{aligned}
\tag{3.28}
$$

and

$$
\begin{aligned}
E_\phi(\mathbf{r}) \;=\; & \jmath\,\omega\mu_0 nI\Bigg\{ \frac{1}{\pi} \sum_{\lambda=0}^{\infty} \frac{4}{2\lambda+1} \sin[(2\lambda+1)\phi] \\
& \int_0^{\infty} \left[\kappa J_{2\lambda}(\kappa\rho) - \frac{2\lambda+1}{\rho}J_{2\lambda+1}(\kappa\rho) \right] \mathcal{F}_{2\lambda+1}(a,b,\kappa)\,\widetilde{g}\,(\kappa,z,h)\sinh(\kappa c)\,d\kappa \\
& - \int_0^{\infty} \kappa J_1(\kappa\rho)\mathcal{F}_0(a,b,\kappa)\,\widetilde{g}\,(\kappa,z,h)\sinh(\kappa c)\,d\kappa \Bigg\}
\end{aligned}
\tag{3.29}
$$

respectively.

3.4   Results

The sensor signals due to a square recess in the bottom surface of a plate of thickness 4.85 mm, Fig. 2, with the racetrack coil above the plate providing the excitation field has been calculated using a volume element code [4]. The dimensions of the recess are 25.4 mm × 25.4 mm × 3 mm. These and other parameters are given in Table 1.

The sensors measure the magnetic field component normal to the surface of the conductor. Fig. 3, compares the variation with probe position of the normal magnetic field at a central sensor. Field values are normalized to a coil current of 1 Amp. The field variation is due to the back surface recess is plotted for three racetrack excitation coils. One has 32 mm straight sections, one has 16 mm straight sections and the other has no straight sections and is thus a circular coil. Results from the zero straight section coil using computer code for the racetrack analysis agree with results for a dedicated circular coil calculation [5]. The absolute value of the z-component of the field found by simulating the response of a 33 element sensor array is shown in Fig. 4.

3.5   Conclusion

The theory for a racetrack coil in the presence of a stratified conductor has been given in two parts based on a formulation using a magnetic dipole representation of the effect of the coil. In the first part the field due to the straight sections of the track are found using a two dimensional Fourier transform, and in the second part, the field due to the semicircular bends of the track are determined using integrals containing Bessel functions. The racetrack coil geometry will be incorporated into a probe design in which an array of magnetic sensors are located along the center line of the track parallel to the straight sections. In this way the local applied field experienced by each sensor is similar yet the probe itself is compact and easy to manipulate.

Bibliography

[1] P. Morse and H. Feshbach, Methods of Theoretical Physics. (McGraw-Hill, New York, 1953) p. 1263.

[2] M. Abramowitz and I. A. Stegun, *Handbook of Mathematical Functions with Formulas, Graphs and Mathematical Tables* (9th printing, Dover, New York, 1970).

[3] D. McA. McKirdy, S. Cochran, G. B. Donaldson and A. McNab, Theoretical Consideration of Fatigue Crack Detection and Characterisation Using SQUID Sensors. In: R Collins W D Dover J R Bowler and K Miya (eds.), Nondestructive Testing of Materials. IOS Press, Amsterdam, p. 185 (1995).

[4] J. R. Bowler, S. A. Jenkins, H. A. Sabbagh and L. D. Sabbagh, J. Appl. Phys. 70, No. 3, p. 1107, 1991.

[5] C.V Dodd and W. E. Deeds, J. Appl. Phys., 39, 2829, 1968.

Table 3.2: Test Parameters for magnetic sensor measurements on a hidden surface material-loss specimen.

Coil	
Outer radius	10.625 mm
Inner radius	1.6875 mm
Axial length	4.98 mm
Nominal lift-off	2.5825 mm
Number of turns	337 ± 1 mm
Number of sensors	33
Height of sensors	0.869 mm
Distance between sensors	2.0 mm
Frequency	2000 Hz
Plate	
Conductivity	1.82×10^7 S/m
Thickness	4.85 mm
Flaw	
Length	25.4 mm
Width	25.4 mm
Depth	3.00 mm
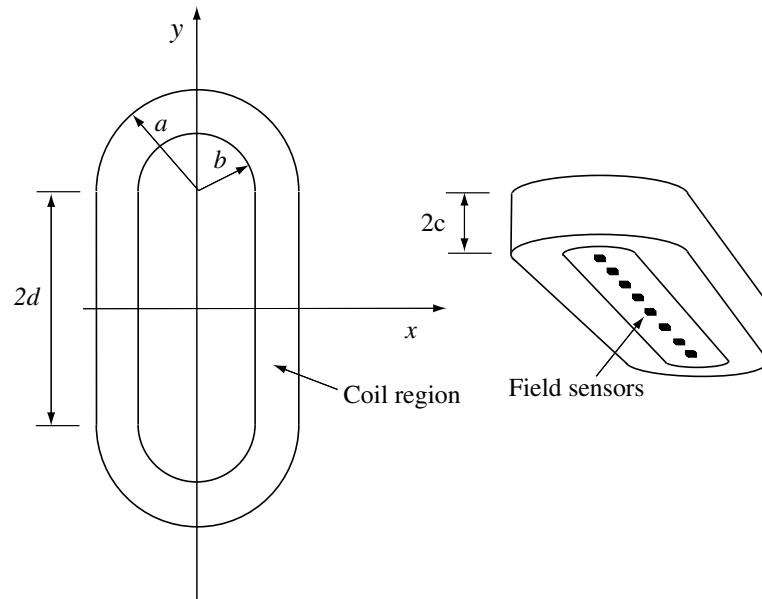
FIG. 1. Racetrack probe showing coil geometry and magnetic field sensor array.
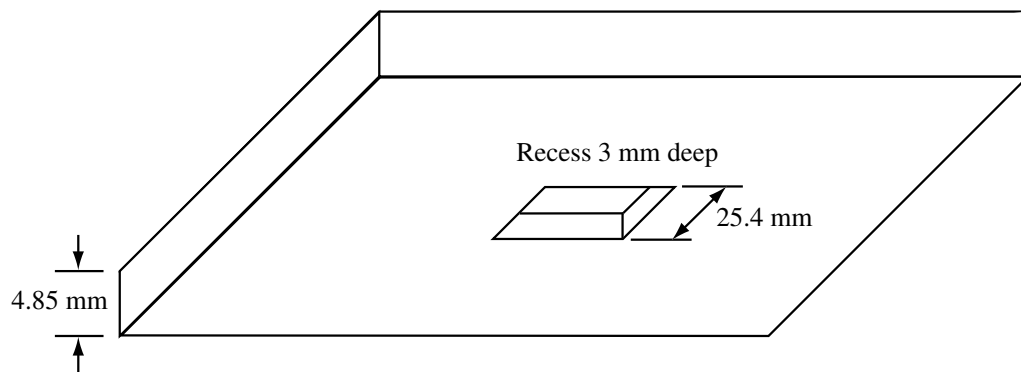
FIG. 2. Conducting plate with a square recess.
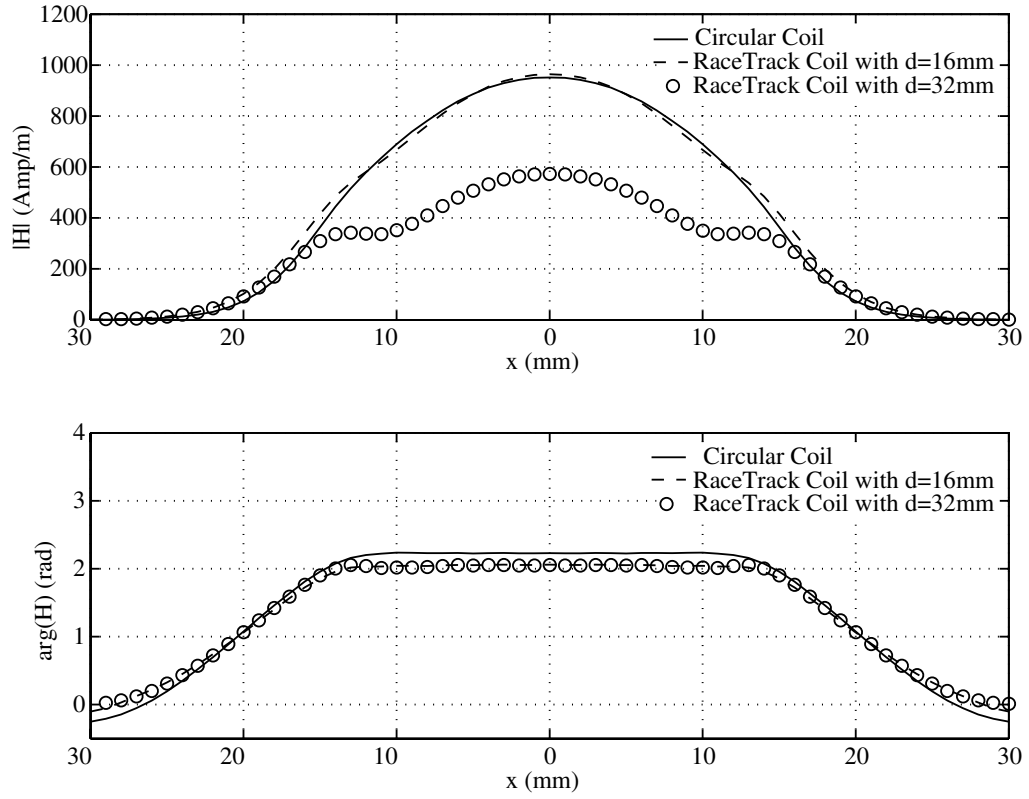
FIG. 3. Variation with probe position of the magnitude and phase of the magnetic field at the site of a central sensor 0.89 mm from the surface of the material.
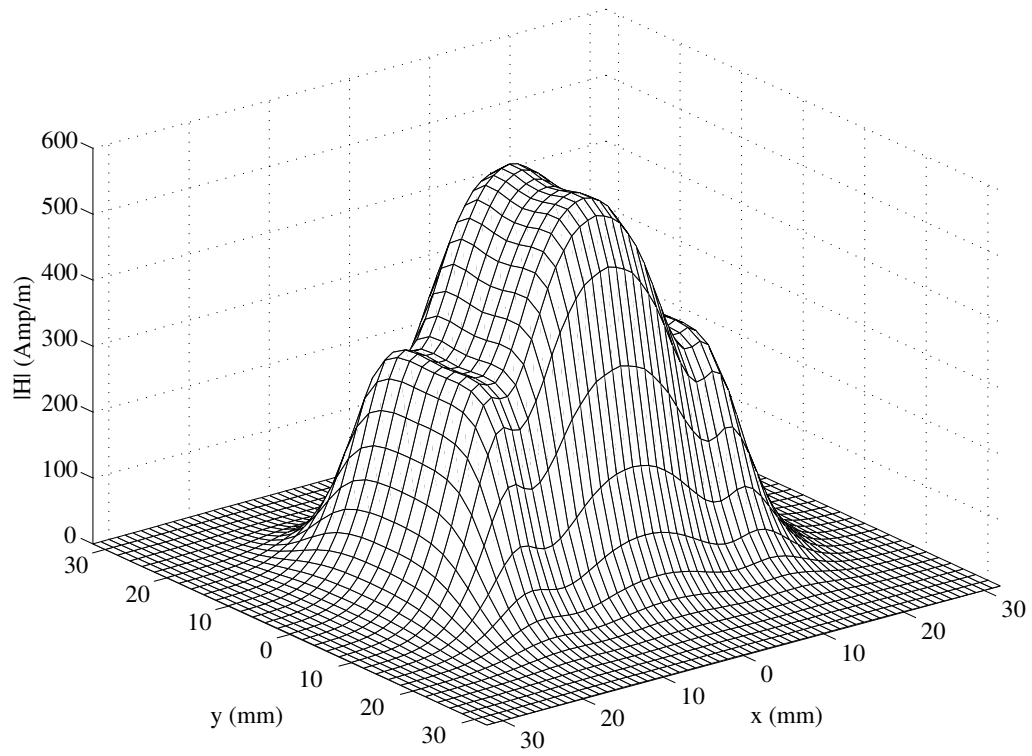
FIG. 4. Magnitude of the magnetic field at 32 sensor sites due to racetrack coil excitation of a metal plate containing a back surface recess, Fig. 2. The excitation frequency is 2000 Hz, $2d = 64$ mm (see Fig. 1) and the other probe dimensions are as given in Table I.

Article 4

Dyadic Green's Functions for the Calculation of Eddy Currents in Planar Stratified Conductors

4.1 Introduction

The use of dyadic Green's functions for electromagnetic field problems is discussed in reference [1]. The dyadic Green's function for an infinite stratified conductor in the quasi-static limit can be derived using scalar decomposition. The approach [2] reduces the problem to one of finding scalar transverse magnetic (TM) and transverse electric (TE) components of the field in a multi–layered planar structure. Here we give specific results for a half-space conductor and an infinite slab. The tedious but straightforward steps describing the derivation of the TE and TM scalar Green's functions satisfying the appropriate continuity conditions at layer interfaces are omitted.

4.2 Dyadic Green's Function

4.2.1 Scalar Decomposition

The required dyadic Green's function, representing physically the electric field due to a singular electric source, can be written in the form [2][3]

$$\mathcal{G}(\mathbf{r}|\mathbf{r}') = \frac{1}{k^2}(\nabla \times \nabla \times \hat{z})(\nabla' \times \nabla' \times \hat{z})U'(\mathbf{r}|\mathbf{r}') + (\nabla \times \hat{z})(\nabla' \times \hat{z})U''(\mathbf{r}|\mathbf{r}'). \qquad (4.1)$$

where the 'wavenumber' k having a positive real part is found from $k^2 = i\omega\mu\sigma$. This scalar form is valid everywhere except at the singularity [2] but this need not concern us because the correct representation of the singularity is well know and in any case will be reintroduced later [by using eq (4.8)]. The numerical treatment of the hyper-singularity will not be discussed here however reference [4] covers this topic adequately.

The functions U' and U'' are related to transverse magnetic (TM) and transverse electric (TE) Green's functions by

$$\left[\begin{array}{c} G'(\mathbf{r}|\mathbf{r}') \\ G''(\mathbf{r}|\mathbf{r}') \end{array} \right] = -\nabla_t^2 \left[\begin{array}{c} U'(\mathbf{r}|\mathbf{r}') \\ U''(\mathbf{r}|\mathbf{r}') \end{array} \right]. \qquad (4.2)$$

In homogeneous regions, the scalar Green's functions, G' and G'', satisfy the inhomogeneous Helmholtz equation:

$$(\nabla^2 + k^2) \left[\begin{array}{c} G'(\mathbf{r}|\mathbf{r}') \\ G''(\mathbf{r}|\mathbf{r}') \end{array} \right] = - \delta(\mathbf{r} - \mathbf{r}') \qquad (4.3)$$

subject to appropriate interface conditions which are derived from the continuity of the tangential electric and magnetic field.

4.2.2 Interface Conditions

Specifically, the continuity of the tangential electric field means that[3]

---

[3]The square bracket is used to denote the jump of a function at an interface. Thus the expression $[f] = j$ means that the jump (discontinuous change) in f at an interface is j. If it happens that [f]=0 at an interface then it means that f is continuous there.

$$\left[\frac{\partial G'}{\partial z}\right] = 0 \quad \text{and} \quad [\mu G''] = 0 \tag{4.4}$$

Similarly the continuity of $\mathbf{H}_t$ implies that

$$[\sigma G'] = 0 \quad \text{and} \quad \left[\frac{\partial G''}{\partial z}\right] = 0. \tag{4.5}$$

The continuity conditions are applied to determine the Fourier transform of the TE and TM Green's functions.

4.2.3 Fourier Representation

Using a two-dimensional Fourier representation, denoted by a tilde, we define

$$\widetilde{G}(z, z') = \int_{-\infty}^{\infty} \int_{-\infty}^{\infty} G(\mathbf{r}|\mathbf{r}')e^{-iu(x-x')-iv(y-y')}\,du\,dv, \tag{4.6}$$

with the inverse

$$G(\mathbf{r}|\mathbf{r}') = \frac{1}{(2\pi)^2} \int_{-\infty}^{\infty} \int_{-\infty}^{\infty} \widetilde{G}(z, z')e^{iu(x-x')+iv(y-y')}\,du\,dv, \tag{4.7}$$

where the tilde implies dependence on the Fourier space coordinates u and v.

4.2.4 Further Useful Dyadic Forms

The scalar decomposition, (4.1) is transformed to more convenient forms by using the following two equations which can be derived using identities give on page 18 of the text by Felsen and Marcuvitz [2].

$$\left[\mathcal{I} + \frac{1}{k^2}\nabla\nabla\right]G_{\Upsilon}(\mathbf{r}|\mathbf{r}') = \frac{1}{k^2}(\nabla\times\nabla\times\hat{z})(\nabla'\times\nabla'\times\hat{z})U_{\Upsilon}(\mathbf{r}|\mathbf{r}') + (\nabla\times\hat{z})(\nabla'\times\hat{z})U_{\Upsilon}(\mathbf{r}|\mathbf{r}') \tag{4.8}$$

where the subscript Υ denotes , $x - x'$, $y - y'$, $z - z'$ dependence. Although the scalar form (4.1) and the equivalence (4.8) are not valid at the singular point, our final result will contain the correct representation of the singularity in the form of the left hand side of (4.8). The second equation for transforming (4.1) is

$$\left[\mathcal{I}' - \frac{1}{k^2}\nabla\nabla'\right]G_{\Lambda}(\mathbf{r}|\mathbf{r}'') = -\frac{1}{k^2}(\nabla\times\nabla\times\hat{z})(\nabla'\times\nabla'\times\hat{z})U_{\Lambda}(\mathbf{r}|\mathbf{r}'') + (\nabla\times\hat{z})(\nabla'\times\hat{z})U_{\Lambda}(\mathbf{r}|\mathbf{r}'') \tag{4.9}$$

where the subscript Λ denotes a $x - x'$, $y - y'$, $z + z'$ dependence and $\mathcal{I}' = \hat{x}\hat{x} + \hat{y}\hat{y} - \hat{z}\hat{z}$.

4.2.5 Evaluation of the Scalar Green's Function

Suppose we have a multilayered structure then we need a subscript to identify which layer is being referred to. We shall not however introduce this layer subscript since the details will be omitted. However, to summarize briefly, we locate the singular source in one of these layers. Then proceed as follows:

- Write the Fourier transform of the solution of (4.3) as

$$\widetilde{G}(z, z') = A(\kappa)e^{-\gamma z} + B(\kappa)e^{\gamma z}$$

for each layer.

- Apply the boundary conditions to find all the A and B coefficients. If the number of layers above and below the source layer is arbitrary then the relationships between the coefficients can be expressed recursively [5] as is done for example, by Dodd, Cheng and Deeds [6] for the field in a multilayered cylindrical structure.

- Use (4.1) (4.8) and (4.9) to express the dyadic Green's function in a form suitable for computation.

Two examples are given below.

4.3 Homogeneous Half-Space

4.3.1 Scalar Forms

A simple example of the general layered domain is one where the source is located in a homogeneous half-space conductor (z'¡0) adjoining a non-conducting half-space (z¿0). For the field in the conducting half-space ($z < 0$),

$$
\begin{aligned}
\widetilde{G}'(z,z') &= \frac{1}{2\gamma}\left[e^{-\gamma|z-z'|} - e^{\gamma(z+z')}\right] \\
\widetilde{G}''(z,z') &= \frac{1}{2\gamma}\left[e^{-\gamma|z-z'|} + \frac{\gamma-\kappa}{\gamma+\kappa}e^{\gamma(z+z')}\right],
\end{aligned}
\tag{4.10}
$$

with $\gamma^2 = \kappa^2 - k^2$ and $\kappa^2 = u^2 + v^2$, taking positive real roots in each case.

As in more complicated cases, such as the slab below, it is useful to express the scalar Green's functions, for both TE and TM modes, as (suppressing the primes distinguishing TE and TM modes)

$$
\widetilde{G}(z|z') = \widetilde{G}_\Upsilon(z|z') + \widetilde{G}_\Lambda(z|z'),
\tag{4.11}
$$

where, the $z - z'$ dependent Green's function $G_\Upsilon(z|z')$ is just the unbounded domain term, G_0 say,

$$
\widetilde{G}_\Upsilon(z|z') = \frac{1}{2\gamma}e^{-\gamma|z-z'|} = \widetilde{G}_0(z|z'),
\tag{4.12}
$$

whereas the $z + z'$ dependent term is

$$
\widetilde{G}_\Lambda = \frac{1}{2\gamma}\Gamma(\kappa)e^{\gamma(z+z')} = -\widetilde{G}_0(z|-z') + \widetilde{V}(z|z')
\tag{4.13}
$$

where

$$
\widetilde{V}(z|z') = \frac{1}{2\gamma}[\Gamma(\kappa)+1]e^{\gamma(z+z')}
\tag{4.14}
$$

In this way, the modes are distinguished by having different 'reflection' coefficients:

$$
\Gamma' = -1 \qquad \text{and} \qquad \Gamma'' = \frac{\gamma-\kappa}{\gamma+\kappa}
\tag{4.15}
$$

for a nonmagnetic conductor. Note that because the TM reflection coefficient is -1 $\widetilde{V}' = 0$.

4.3.2 Dyadic Form

Using (4.1), (4.8) and (4.9) the dyadic Green's function for the half-space conductor is written as

$$\mathcal{G}(\mathbf{r}|\mathbf{r}') = \left[\mathcal{I} + \frac{1}{k^2}\nabla\nabla\right]G_0(\mathbf{r}|\mathbf{r}') + \left[\mathcal{I}' - \frac{1}{k^2}\nabla\nabla'\right]G_0(\mathbf{r}|\mathbf{r}'') + (\nabla\times\hat{z})(\nabla'\times\hat{z})V''(\mathbf{r}|\mathbf{r}') \quad (4.16)$$

where $\mathbf{r}'' = \mathbf{r}' - 2z\hat{z}$ is the image point and

$$G_0(\mathbf{r}|\mathbf{r}') = \frac{e^{ik|\mathbf{r}-\mathbf{r}'|}}{4\pi|\mathbf{r}-\mathbf{r}'|} \tag{4.17}$$

is the familiar free space scalar Green's function for the Helmholtz equation.

4.4 Conducting Slab

4.4.1 Scalar Forms

For a conducting slab thickness d we again adopt the form given in equation (4.11) for both TE and TM modes where we now have

$$\widetilde{G}_\Upsilon(z|z') = \frac{1}{2\gamma}\left\{e^{-\gamma|z-z'|} + e^{-\gamma(z-z'+2d)} + e^{\gamma(z-z'-2d)} + \Upsilon(\kappa)\left[e^{\gamma(z-z'-2d)} + e^{-\gamma(z-z'+2d)}\right]\right\}.$$
$$\tag{4.18}$$

with a reminder that the chosen roots of $\gamma^2 = \kappa^2 - k^2$ and $\kappa^2 = u^2 + v^2$ have positive real parts. For a conducting slab in air, reflection from top and bottom surfaces involves the same reflection coefficient, hence, with the upper sign for the TE mode and the lower sign for the TM mode

$$\widetilde{G}_\Lambda(z|z') = \frac{1}{2\gamma}\left\{\pm e^{-\gamma(z+z')} \pm e^{\gamma(z+z'-2d)} + \Lambda(\kappa)\left[e^{\gamma(z+z'-2d)} + e^{-\gamma(z+z')}\right]\right\}, \tag{4.19}$$

where

$$\Upsilon(\kappa) = \frac{\Gamma^2}{1 - \Gamma^2 e^{-2\gamma d}} - 1$$

$$\Lambda(\kappa) = \frac{\Gamma}{1 - \Gamma^2 e^{-2\gamma d}} \mp 1. \tag{4.20}$$

Note that once again

$$\Gamma' = -1 \quad \text{and} \quad \Gamma'' = \frac{\gamma - \kappa}{\gamma + \kappa} \tag{4.21}$$

for a nonmagnetic slab.

In (4.18) the second and third term represent the field due to images created by reflection at the upper and lower surface of the slab. Similarly the first two terms in (4.19) represent the field due t single reflections at upper and lower surfaces. The image terms are separated in order that the computation of matrix element may be performed on these terms using the same code that is used for the the contribution from the free space Green's function. This avoids taking them into account via the alternative, Fourier-Bessel integral, representation.

4.4.2 Dyadic Forms

To assemble the explicit slab dyadic Green's function, we sub the explicit form of the scalar Green's functions into equation (4.1). The result is then manipulated using (4.8) and (4.9) (see Felsen and Marcuvitz [2], p18) to give

$$\mathcal{G}(\mathbf{r}|\mathbf{r}') = \mathcal{G}_\Upsilon(\mathbf{r}|\mathbf{r}') + \mathcal{G}_\Lambda(\mathbf{r}|\mathbf{r}'), \tag{4.22}$$

where

$$\begin{aligned}\mathcal{G}_\Upsilon(\mathbf{r}|\mathbf{r}') = \mathcal{G}^{(0)}(\mathbf{r}|\mathbf{r}') \quad &+ \quad \mathcal{G}^{(0)}(\mathbf{r}|\mathbf{r}_{+-}) + \mathcal{G}^{(0)}(\mathbf{r}|\mathbf{r}_{-+}) \\ &+ \quad \mathcal{W}_-(\mathbf{r}|\mathbf{r}') + \nabla \times \hat{z}[\nabla' \times \hat{z}V_-(\mathbf{r}|\mathbf{r}')]\end{aligned} \tag{4.23}$$

and

$$\begin{aligned}\mathcal{G}_\Lambda(\mathbf{r}|\mathbf{r}') \quad = \quad &\mathcal{G}^{(i)}(\mathbf{r}|\mathbf{r}_+) + \mathcal{G}^{(i)}(\mathbf{r}|\mathbf{r}_-) \\ + \quad &\mathcal{W}_+(\mathbf{r}|\mathbf{r}') + \nabla \times \hat{z}[\nabla' \times \hat{z}V_+(\mathbf{r}|\mathbf{r}')].\end{aligned} \tag{4.24}$$

The new variables are defined as follows:

$$\begin{aligned}\mathbf{r}_+ &= \mathbf{r}' - 2(z'-d)\hat{z} \\ \mathbf{r}_- &= \mathbf{r}' - 2(z')\hat{z} \\ \mathbf{r}_{+-} &= \mathbf{r}' - 2d\hat{z} \\ \mathbf{r}_{-+} &= \mathbf{r}' + 2d\hat{z}.\end{aligned} \tag{4.25}$$

$\mathcal{G}_0(\mathbf{r}|\mathbf{r})$ is the dyadic Green's function for an unbounded conductor given by

$$\mathcal{G}^{(0)}(\mathbf{r}|\mathbf{r}') = [\mathcal{I} + \frac{1}{k^2}\nabla\nabla]G_0(\mathbf{r}|\mathbf{r}'), \tag{4.26}$$

with

$$G_0(\mathbf{r}|\mathbf{r}') = \frac{e^{ik|\mathbf{r}-\mathbf{r}'|}}{4\pi|\mathbf{r}-\mathbf{r}'|}. \tag{4.27}$$

The remaining terms in (4.23) are due to reflection at the upper and lower surfaces of the source stratum. The first two of these remaining terms are double refection image terms. In (4.24) we find that two single reflection image terms given by

$$\mathcal{G}^{(i)}(\mathbf{r}|\mathbf{r}_\pm) = [\mathcal{I}' - \frac{1}{k^2}\nabla\nabla']\phi(\mathbf{r}|\mathbf{r}_\pm), \tag{4.28}$$

where $\mathcal{I}' = \hat{x}\hat{x} + \hat{y}\hat{y} - \hat{z}\hat{z}$. The other terms are defined as follows:

$$\mathcal{W}_-(\mathbf{r}|\mathbf{r}') = [\mathcal{I} + \frac{1}{k^2}\nabla\nabla]W_-(\mathbf{r}|\mathbf{r}'), \tag{4.29}$$

$$\mathcal{W}_+(\mathbf{r}|\mathbf{r}') = [\mathcal{I}' - \frac{1}{k^2}\nabla\nabla']W_+(\mathbf{r}|\mathbf{r}'), \tag{4.30}$$

where

$$W_-(\rho, z, z') = \frac{1}{2\pi}\int_0^\infty \frac{1}{2\gamma}\Upsilon'(\kappa)\left[e^{\gamma(z-z'-2d)} + e^{-\gamma(z-z'+2d)}\right]J_0(\kappa\rho)\kappa d\kappa \tag{4.31}$$

$$W_+(\rho, z, z') = -\frac{1}{2\pi} \int_0^\infty \frac{1}{2\gamma} \Lambda'(\kappa) \left[e^{\gamma(z+z'-2d)} + e^{-\gamma(z+z')} \right] J_0(\kappa\rho)\kappa d\kappa \tag{4.32}$$

$$V_-(\rho, z, z') = \frac{1}{2\pi} \int_0^\infty \frac{1}{2\kappa\gamma} \left[\Upsilon''(\kappa) - \Upsilon'(\kappa) \right] \left[\left[e^{\gamma(z-z'-2d)} + e^{-\gamma(z-z'+2d)} \right] J_0(\kappa\rho) d\kappa \tag{4.33}$$

$$V_+(\rho, z, z') = \frac{1}{2\pi} \int_0^\infty \frac{1}{2\kappa\gamma} \left[\Lambda''(\kappa) + \Lambda'(\kappa) \right] \left[e^{\gamma(z+z'-2d)} + e^{-\gamma(z+z')} \right] J_0(\kappa\rho) d\kappa, \tag{4.34}$$

where $\rho = [(x-x')^2 + (y-y')^2]^{1/2}$.

Bibliography

[1] C.T. Tai, *Dyadic Green Functions in Electromagnetic Theory*, 2nd Edition, IEEE Press, New York, 1994.

[2] L. B. Felsen and N. Marcuvitz, *Radiation and Scattering of Waves.* New Jersey: Prentice-Hall, 1972.

[3] J. R. Bowler, J. Appl. Phys. **61** (3), 833 1987.

[4] S. Lee, J. B. Boersma, C. Law and G. A. Deschamps, *Singularity in Green's function and its numerical evaluation, IEEE Trans. Antennas Propagat.,* Vol. AP-28, No.3, pp311-317, 1986.

[5] J. R. Bowler, "The Calculation of Eddy Current Distributions Using Tensor Green's Functions," supported by The Defence Research Agency, Farnborough under EMR Contract Number ER1/9/4/2064/115 XR/STR (1994).

[6] C V Dodd C C Cheng and W E Deeds, J. Appl. Phys, Vol 45, N0 2, Feb 1974.

Article 5

Edge Elements Based Numerical Computation of Dipole Density in Eddy Current Testing Problems

Guglielmo Rubinacci and Antonello Tamburrino

DAEIMI

Laboratory of Computational Electromagnetics
and Electromagnetic Nondestructive Evaluation

Università degli Studi Cassino, Via G. Di Biasio, 43 Cassino, I-03043

Summary

1. Introduction
2. Mathematical model
3. Numerical model
   Appendix A: edge element shape functions
   Appendix B: Tree-Cotree Decomposition
   Appendix C: integration of the hyper-singular term
   References

1. Introduction

This report presents an edge elements based numerical method for computing the dipole density $\mathbf{P}$ arising from the interaction of eddy currents with a flaw in a conductive slab.

The dipole density appears in the region Ω_f occupied by the flaw and it can be determined by solving an integral equation in Ω_f. This is a great advantage from the numerical viewpoint because it requires the discretization only of Ω_f, which is generally a small part of the whole conductive domain Ω_0. However, the electric-electric dyadic Green's function in the presence of the conductive material (without flaw) is required and the kernel of the resulting integral equation is hyper-singular. Moreover, the electric-electric dyadic Green's function is known only for canonical geometries such as, for instance, the homogenous slab.

Assuming that the conductivity of the flaw is constant, the dipole density is solenoidal and can thus be represented as the curl of a vector potential $\mathbf{U}$, which we term the dipole vector potential. The numerical formulation is based on the Galerkin method applied to the integral equation satisfied by $\mathbf{P}$ and expanding $\mathbf{U}$ as the linear combination of edge element based shape functions. The uniqueness of the dipole vector potential is numerically imposed by means of the tree-cotree decomposition of the finite elements mesh used to build the edge element shape functions. This numerical formulation automatically takes into account the solenoidality of $\mathbf{P}$ and thus allows the number of unknowns to be reduced with respect to the method of moment when applied on the same mesh, and makes it possible to improve the rate of convergence of the numerical solution. Moreover, by taking into account the solenoidality of $\mathbf{P}$, the volume integral arising from the hyper-singular part of the dyadic Green's function is reduced to a surface integral containing the scalar Green's function as its kernel.

2. Mathematical model

Let us consider a conductive slab made of a linear, isotropic, non-dispersive, non-magnetic, non-dielectric and homogenous material of conductivity $\boldsymbol{s}_0$ hosted in free space. Let us assume that the flaw is a volumetric flaw occupying the three dimensional domain Ω_f and that the conductivity of the flaw assumes the constant value $\boldsymbol{s}_f$ (see figure 2.1).

The governing equations are (assuming the e^{-jwt} time-dependence):

$$\nabla \times \mathbf{E} = jw\boldsymbol{n}_0 \mathbf{H}$$
$$\nabla \times \mathbf{H} = \mathbf{J}_0 + \boldsymbol{s}(\mathbf{r})\mathbf{E} - jw\boldsymbol{e}_0\mathbf{E}$$
$$\nabla \cdot \mathbf{E} = \frac{\boldsymbol{r}}{\boldsymbol{e}_0} \tag{2.1}$$
$$\nabla \cdot \mathbf{H} = 0$$

together with the radiation condition at infinity and[1]

$$\boldsymbol{s}(\mathbf{r}) = \begin{cases} \boldsymbol{s}_0(\mathbf{r}) \text{ in } \Re^3 \setminus \Omega_f \\ \boldsymbol{s}_f \text{ in } \Omega_f \end{cases} \tag{2.2}$$

$$\boldsymbol{s}_0(\mathbf{r}) = \begin{cases} \boldsymbol{s}_0 \text{ in } \Omega_0 \\ 0 \text{ in } \Re^3 \setminus \Omega_0 \end{cases} \tag{2.3}$$

where Ω_0 is the domain occupied by the conductor without the flaw.

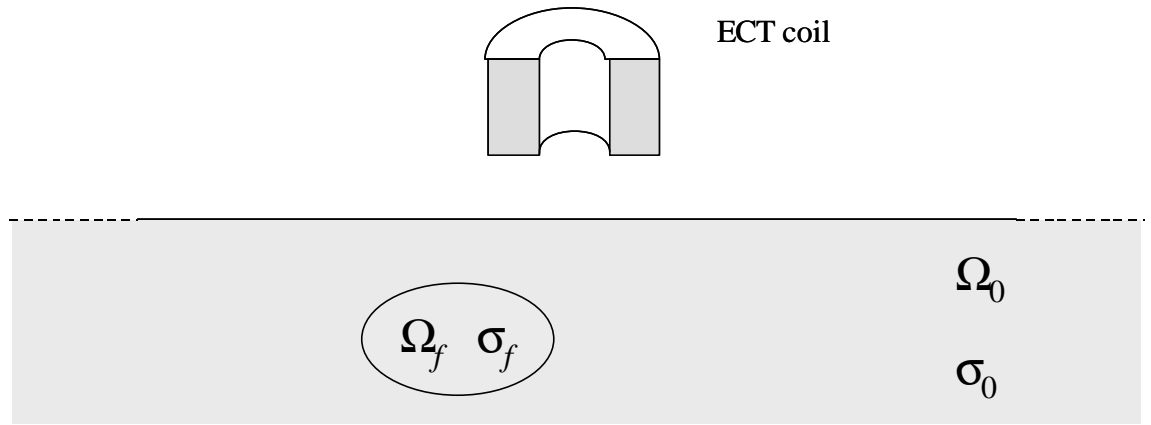Figure 2.1. The reference geometry. Ω_0 is the spatial region containing a homogeneous conductive slab of conductivity $\boldsymbol{s}_0$. A homogenous anomaly of conductivity $\boldsymbol{s}_f$ occupies the volumetric domain Ω_f.

---

[1] Notice that the symbol $\boldsymbol{s}_0(\mathbf{r})$ stands for the function defined by (2.3) whereas $\boldsymbol{s}_0$ stands for the constant.

By introducing the dipole density vector field **P** defined as:

$$\mathbf{P}(\mathbf{r}) \triangleq (\boldsymbol{s}(\mathbf{r}) - \boldsymbol{s}_0(\mathbf{r}))\mathbf{E}(\mathbf{r}), \tag{2.4}$$

Ampere's law can be written as

$$\nabla \times \mathbf{H} = \mathbf{J}_0 + \mathbf{P} + \boldsymbol{s}_0(\mathbf{r})\mathbf{E} - jw\boldsymbol{e}_0\mathbf{E} \tag{2.5}$$

showing that **P** acts as a secondary source of the electromagnetic field produced without the flaw (i.e. $\Omega_f = \Phi$).

Notice that **P** is different from zero only in Ω_f ($\boldsymbol{s}(\mathbf{r}) = \boldsymbol{s}_0(\mathbf{r})$ in $\mathfrak{R}^3 \setminus \Omega_f$), the anomalous region. As is well known (see [1]) **P** in Ω_f can be found by solving the following integral equation:

$$\mathbf{P}(\mathbf{r}) = \mathbf{P}^{(i)}(\mathbf{r}) + (\boldsymbol{s}_f - \boldsymbol{s}_0) jw\boldsymbol{m}_0 \int_{\Omega_f} \mathbf{G}^{ee}(\mathbf{r} \mid \mathbf{r}')\mathbf{P}(\mathbf{r}')d\mathbf{r}', \forall \mathbf{r} \in \Omega_f \tag{2.6}$$

where $\mathbf{P}^{(i)} = (\boldsymbol{s}_f - \boldsymbol{s}_0)\mathbf{E}^{(i)}$, $\mathbf{E}^{(i)}$ is the electric field due to $\mathbf{J}_0$ when $\boldsymbol{s}_0 = \boldsymbol{s}_f$ (i.e. without the flaw) and $\mathbf{G}^{ee}$ is the electric-electric dyadic Green's function for $\boldsymbol{s}_f = \boldsymbol{s}_0$. Notice that $\mathbf{G}^{ee}$ is the solution of:

$$\nabla \times \nabla \times \mathbf{G}^{ee}(\mathbf{r} \mid \mathbf{r}') - jw\boldsymbol{m}_0\boldsymbol{s}_0(\mathbf{r})\mathbf{G}^{ee}(\mathbf{r} \mid \mathbf{r}') = \mathbf{I}\boldsymbol{d}(\mathbf{r} - \mathbf{r}') \tag{2.7}$$

together with the radiation condition at infinity and $\mathbf{I} = \hat{x}\hat{x} + \hat{y}\hat{y} + \hat{z}\hat{z}$ is the identity operator expressed in terms of unit vectors.

The integral equation (2.6) is interesting because its numerical solution requires the discretization of Ω_f only.

The property underlying the numerical scheme is that **P** is solenoidal in $\overset{\circ}{\Omega}_f$, the interior of Ω_f. In fact, by assuming that there is no impressed charge density in Ω_f, i.e. $\nabla \cdot \mathbf{J}_0 = 0$ in $\overset{\circ}{\Omega}_f$, from Ampere's law (2.1) it follows that

$$\nabla \cdot \mathbf{E} = 0 \text{ in } \overset{\circ}{\Omega}_f \tag{2.8}$$

thus from (2.5)

$$\nabla \cdot \mathbf{P} = (\boldsymbol{s}_f - \boldsymbol{s}_0)\nabla \cdot \mathbf{E}$$
$$= 0 \text{ in } \overset{\circ}{\Omega}_f . \tag{2.9}$$

Notice that for given $\boldsymbol{s}_0, \boldsymbol{s}_f \in (0, +\infty)$ nothing can be said on the normal and tangential components of **P** on $\partial\Omega_f$.

The solenoidality of P in $\overset{\circ}{\Omega}_f$ can be automatically taken into account by introducing the dipole vector potential **U** defined by:

$$\mathbf{P} = \nabla \times \mathbf{U}. \tag{2.10}$$

Notice that (2.9) specifies only the curl of $\mathbf{U}$ therefore the uniqueness of $\mathbf{U}$ has to be imposed by gauging $\mathbf{U}$ as shown in Appendix B.

3. Numerical model

The numerical model proposed in this section is obtained by applying Galerkin's method to eq. (2.6). The unknown is the dipole vector potential $\mathbf{U}$ which we represent as the linear combination of edge element based shape functions, i.e. $\mathbf{U} = \sum_e U_e \mathbf{N}_e$ where the $\mathbf{N}_e$'s are edge element based shape functions and e represents an edge of the mesh (see Appendix A). Specifically, the sum is restricted to the edges of a cotree of the finite element to numerically impose the uniqueness of $\mathbf{U}$ (see Appendix B).

The unknown dipole density (see 2.10) is represented as:

$$\mathbf{P} = \sum_e U_e \mathbf{P}_e \tag{3.1}$$

where $\mathbf{P}_e$ is expressed in terms of $\mathbf{N}_e$ as:

$$\mathbf{P}_e = \nabla \times \mathbf{N}_e. \tag{3.2}$$

Galerkin's method applied to (2.6) gives:

$$\left(\underline{\underline{\mathbf{R}}} - jw\underline{\underline{\mathbf{L}}} \right)\underline{\mathbf{U}} = \underline{\mathbf{V}}^{(i)} \tag{3.3}$$

where $\underline{\mathbf{U}}$ is the column vector made of the U_e's and[1]

$$\left(\underline{\mathbf{V}}^{(i)} \right)_k \triangleq \int_{\Omega_f} \nabla \times \mathbf{N}_k(\mathbf{r}) \cdot \mathbf{E}^{(i)}(\mathbf{r}) \mathrm{d}\mathbf{r} \tag{3.4}$$

$$\left(\underline{\underline{\mathbf{R}}} \right)_{kj} \triangleq \frac{1}{s_f - s_0} \int_{\Omega_f} \nabla \times \mathbf{N}_k(\mathbf{r}) \cdot \nabla \times \mathbf{N}_j(\mathbf{r}) \mathrm{d}\mathbf{r} \tag{3.5}$$

$$\left(\underline{\underline{\mathbf{L}}} \right)_{kj} \triangleq m_0 \int_{\Omega_f} \int_{\Omega_f} \nabla \times \mathbf{N}_k(\mathbf{r}) \cdot \mathbf{G}^{ee}(\mathbf{r} \mid \mathbf{r}') \cdot \nabla \times \mathbf{N}_j(\mathbf{r}') \mathrm{d}\mathbf{r}' \mathrm{d}\mathbf{r}. \tag{3.6}$$

Notice that the computation of the matrix $\underline{\underline{\mathbf{L}}}$ can be troublesome due to the hyper-singular part of the dyadic Green's function $\mathbf{G}^{ee}$. However, the computation of hyper-singular integrals can be reduced to the computation of surface integrals on $\partial\Omega_f$. In order to show this, we first notice that

$$\mathbf{G}^{ee}(\mathbf{r} \mid \mathbf{r}') = \mathbf{G}_0^{ee}(\mathbf{r} \mid \mathbf{r}') + d\mathbf{G}^{ee}(\mathbf{r} \mid \mathbf{r}') \tag{3.7}$$

---

[1] In (3.4)-(3.6) k and j represent edges of the finite elements mesh.

where $\mathbf{G}_0^{ee}$ is the electric-electric Green's function when the whole space is filled with a conductive material of conductivity $\mathbf{s}_0$ and $d\mathbf{G}^{ee}$ is a continuous function in Ω_0. As is well known [2], $\mathbf{G}_0^{ee}$ is:

$$\mathbf{G}_0^{ee}(\mathbf{r} \mid \mathbf{r}') = \left(\mathbf{I} + \frac{1}{k^2}\nabla\nabla\right)g_0(\mathbf{r} \mid \mathbf{r}') \tag{3.8}$$

where $k^2 = \mathbf{w}^2\mathbf{m}_0(\mathbf{e}_0 + j\mathbf{s}_0/\mathbf{w})$ and g_0 is the scalar Green's function:

$$g_0(\mathbf{r} \mid \mathbf{r}') = \frac{e^{jk|\mathbf{r}-\mathbf{r}'|}}{4\mathbf{p}|\mathbf{r}-\mathbf{r}'|} \tag{3.9}$$

Following (3.7) the matrix $\underline{\underline{\mathbf{L}}}$ is the sum of two terms:

$$\underline{\underline{\mathbf{L}}} = \underline{\underline{\mathbf{L}}}_0 + \underline{\underline{d\mathbf{L}}} \tag{3.10}$$

where

$$\left(\underline{\underline{\mathbf{L}}}_0\right)_{kj} \triangleq \mathbf{m}_0 \int_{\Omega_f} \int_{\Omega_f} \nabla\times\mathbf{N}_k(\mathbf{r})\cdot\mathbf{G}_0^{ee}(\mathbf{r}\mid\mathbf{r}')\cdot\nabla\times\mathbf{N}_j(\mathbf{r}')d\mathbf{r}d\mathbf{r}' \tag{3.11}$$

$$\left(\underline{\underline{d\mathbf{L}}}\right)_{kj} \triangleq \mathbf{m}_0 \int_{\Omega_f} \int_{\Omega_f} \nabla\times\mathbf{N}_k(\mathbf{r})\cdot d\mathbf{G}^{ee}(\mathbf{r}\mid\mathbf{r}')\cdot\nabla\times\mathbf{N}_j(\mathbf{r}')d\mathbf{r}d\mathbf{r}'. \tag{3.12}$$

The computation of $\underline{\underline{d\mathbf{L}}}$ can be carried out by standard numerical integration techniques (the kernel $d\mathbf{G}^{ee}$ is non-singular), whereas the computation of $\underline{\underline{\mathbf{L}}}_0$ requires volume and surface integrals (on $\partial\Omega_f$) with kernel g_0 (see appendix C):

$$\underline{\underline{\mathbf{L}}}_0 = \underline{\underline{\mathbf{L}}}_0^V + \underline{\underline{\mathbf{L}}}_0^S \tag{3.13}$$

$$\left(\underline{\underline{\mathbf{L}}}_0^V\right)_{kj} = \mathbf{m}_0 \int_{\Omega_f} \int_{\Omega_f} \nabla\times\mathbf{N}_k(\mathbf{r})\cdot g_0(\mathbf{r}\mid\mathbf{r}')\nabla\times\mathbf{N}_j(\mathbf{r}')d\mathbf{r}d\mathbf{r}' \tag{3.14}$$

$$\left(\underline{\underline{\mathbf{L}}}_0^S\right)_{kj} = -\frac{\mathbf{m}_0}{k^2} \int_{\partial\Omega_f} \int_{\partial\Omega_f} \hat{\mathbf{n}}(\mathbf{r})\cdot\nabla\times\mathbf{N}_k(\mathbf{r})\, g_0(\mathbf{r}\mid\mathbf{r}')\, \hat{\mathbf{n}}(\mathbf{r}')\cdot\nabla\times\mathbf{N}_j(\mathbf{r}')dS(\mathbf{r}')dS(\mathbf{r})$$

$$\tag{3.15}$$

Notice that the computation of the singular integral involved in (3.14) and (3.15) can be performed by noting that:

$$g_0(\mathbf{r}\mid\mathbf{r}') = \frac{jk}{4\mathbf{p}}e^{jk|\mathbf{r}-\mathbf{r}'|/2}\mathrm{sinc}\left(\frac{k|\mathbf{r}-\mathbf{r}'|}{2}\right) + \frac{1}{4\mathbf{p}|\mathbf{r}-\mathbf{r}'|}. \tag{3.16}$$

where $\mathrm{sinc}(x) \triangleq \dfrac{\sin(x)}{x}$.

The first term in (3.16) corresponds to a non-singular kernel and its integration can be carried out by standard numerical integration techniques, whereas the second term correspond to the static scalar Green's function and its integration can be carried out as showed in [8].

Appendix A: Edge element shape functions

In the finite elements approach, the continuum is divided into a finite number of parts (elements) with a polyhedral shape; every polyhedral is identified by the coordinates of its vertices (the nodes of the discretization). The unknown function $f(\mathbf{r})$ is represented in each element by a polynomial approximation in terms of NP parameters (the degrees of freedom of the solution) and of given shape functions:

$$f(\mathbf{r}) = \sum_{i=1,NP} a_i N_i(\mathbf{r}). \qquad (A.1)$$

Usually, a_i represents the nodal value of f at the i-th node of coordinates $\mathbf{r}_i$ ($a_i = f(\mathbf{r}_i)$); each shape function N_i (nodal function) is locally based and different from zero only in the elements sharing the same node i and NP is the number of nodes in the finite elements mesh. In this way, inter-element continuity can be assured.

In the following, we consider linear 8-node isoparametric brick elements. We recall that the nodal function N_k associated to the k-th node is continuous, piecewise trilinear, with the following properties:

$$
\begin{aligned}
&N_k(\mathbf{r}_k) = 1 \\
&N_k(\mathbf{r}_m) = 0, \quad k \neq m \\
&\sum_{j=1,NP} N_j(\mathbf{r}) = 1, \quad \mathbf{r} \in V_d
\end{aligned}
\qquad (A.2)
$$

where V_d is the finite element discretization of the domain V. Notice that from (A.2) it follows that the nodal functions N_k's are linearly independent.

We recall that in this case the l-th element is the image of the cube $[-1\ 1]\times[-1\ 1]\times[-1\ 1]$ under the mapping M (see Fig. 1) defined by:

$$
\begin{aligned}
x &= \sum_{k \in I_l} N_k(\boldsymbol{x},\boldsymbol{h},\boldsymbol{z}) x_k \\
y &= \sum_{k \in I_l} N_k(\boldsymbol{x},\boldsymbol{h},\boldsymbol{z}) y_k \\
z &= \sum_{k \in I_l} N_k(\boldsymbol{x},\boldsymbol{h},\boldsymbol{z}) z_k
\end{aligned}
\qquad (A.3)
$$

where x,y,z are the global Cartesian co-ordinates of a point Q corresponding to the point Q of local $\boldsymbol{x},\boldsymbol{h},\boldsymbol{z}$ co-ordinates under the mapping M, I_l is the set of (eight) nodes of the l-th element, and x_k, y_k, z_k are the global coordinates of the k-th node. N_k represents the scalar shape function associated with the k-th node[1]:

---

[1] Notice that we use the same symbol for the shape function in the local $(\boldsymbol{x},\boldsymbol{h},\boldsymbol{z})$, local (r_k, s_k, t_k) and global (x,y,z) co-ordinate systems.

$$N_k(\pmb{x},\pmb{h},\pmb{z}) = \frac{1}{8}(1+\pmb{x}\pmb{x}_k)(1+\pmb{h}\pmb{h}_k)(1+\pmb{z}\pmb{z}_k) = r_k s_k t_k \qquad (A.4)$$

where

$$r_k = \frac{1}{2}(1+\pmb{x}\pmb{x}_k), \quad s_k = \frac{1}{2}(1+\pmb{h}\pmb{h}_k), \quad t_k = \frac{1}{2}(1+\pmb{z}\pmb{z}_k) \qquad (A.5)$$

In this way, the k-th node has local co-ordinates $r_k = s_k = t_k = 1$ in the r_k, s_k, t_k local system of co-ordinates.
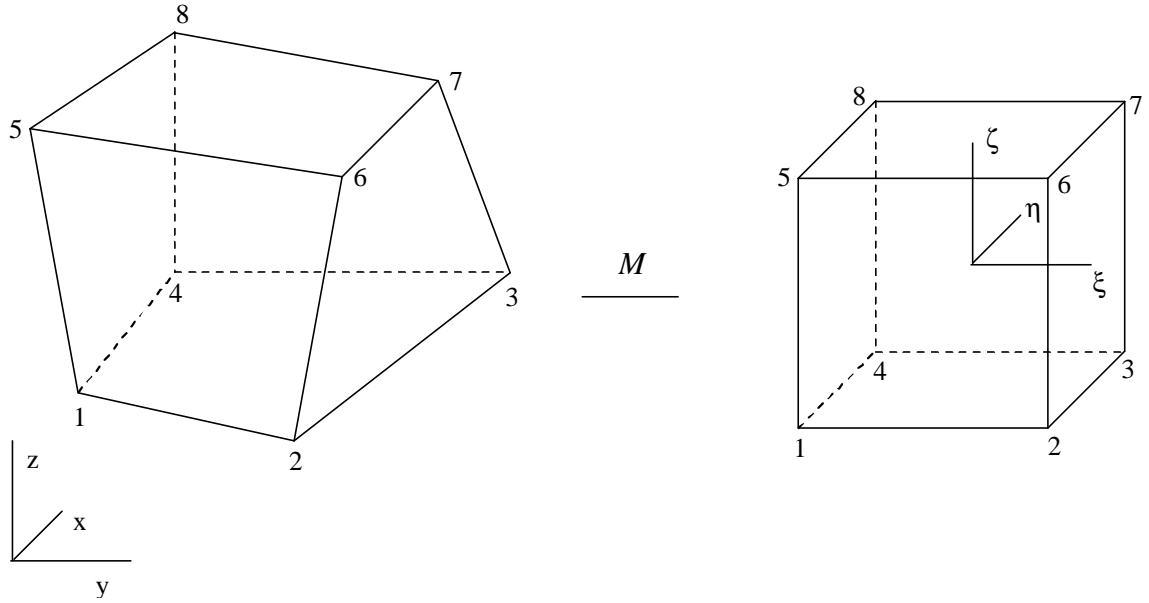

Fig. A.1. The mapping M transforms the cube into the hexahedron. The local co-ordinates of nodes 1 and 7 are (-1,-1,-1) and (1,1,1), respectively.
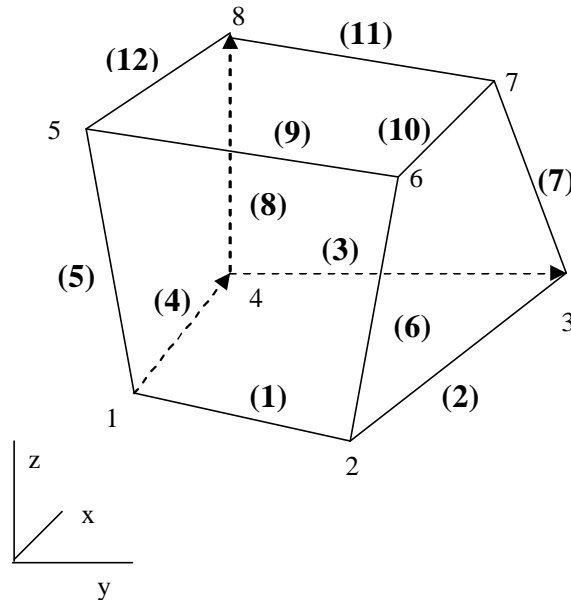

Fig. A.2. The degrees of freedom in the edge elements are associated with the oriented edges of the finite elements mesh
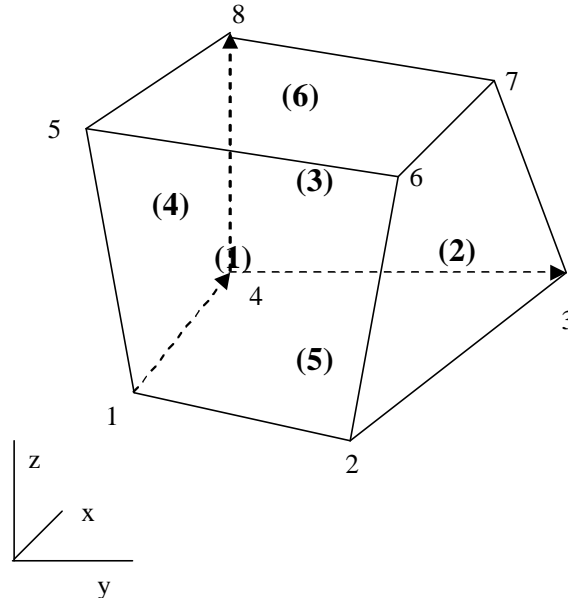
Fig. A.3. The (local) numbering scheme for the faces.

The degrees of freedom of the edge elements are associated with the tangential components along the edges of the elements of a the vector field to be represented (see fig. 2) [3]:

$$\mathbf{U} = \sum_{e=1,E} U_e \mathbf{N}_e \tag{A.6}$$

The shape function associated with the edge $e=\{i, j\}$, connecting the i-th and j-th nodes along ξ is[1] [4]:

$$\mathbf{N}_e = \frac{1}{8}(1 + \boldsymbol{h}\boldsymbol{h}_e)(1 + \boldsymbol{z}\boldsymbol{z}_e)\nabla \boldsymbol{x} = s_e t_e \nabla r_e \tag{A.7}$$

where $\boldsymbol{h}_e$ and $\boldsymbol{z}_e$, equal to ± 1, are the local co-ordinates of the edge e and r_e, s_e, t_e is the local frame where the edge e is described as $s_e=t_e=1$, $r_e \in [0,1]$. The shape functions for edges running along $\boldsymbol{h}$ and $\boldsymbol{z}$ are obtained by cyclic permutations while $\mathbf{N}_{e'} = -\mathbf{N}_e$ when $e'=\{j, i\}$.

We notice that:

- The line integral of $\mathbf{N}_e$ along the edge e (from node i to node j) is one:

$$\int_{\{i,j\}} \mathbf{N}_e \cdot d\mathbf{l} = 1 \tag{A.8}$$

- The line integral of $\mathbf{N}_e$ is zero along any other edge $\{l,k\} \neq \{i, j\}$ and $\{k,l\} \neq \{i, j\}$:

---

[1] The ordered pair $\{i, j\}$ represents the oriented edge of the finite elements mesh directed from node i to node j.

$$\int\limits_{\{l,k\}} \mathbf{N}_e \cdot d\mathbf{l} = 0 \qquad (A.9)$$

- The tangential components of $\mathbf{N}_e$ are continuous across the face of adjacent elements since the scalar functions N_k are continuous.
- The normal components of $\mathbf{N}_e$ are not necessarily continuous.
- $\mathbf{N}_e$ and ∇N_k belong to the same functional space: the gradient of a nodal shape function is given by a linear combination of the edge shape functions having in common that node:

$$\nabla N_k = \sum_{e=1,E} G_{ek} \mathbf{N}_e \qquad (A.10)$$

where E is the number of edges of the mesh and $\underline{\mathbf{G}}$ is the $E \times NP$ incidence matrix defined by:

$$G_{em} = \begin{cases} +1 \text{ if } e = \{i,j\} \text{ and } m = j \\ -1 \text{ if } e = \{i,j\} \text{ and } m = i \\ 0 \text{ otherwise} \end{cases} \qquad (A.11)$$

Similarly, a set of shape functions $\mathbf{S}_f$ associated with the faces of the elements can be introduced. In this case, the flux of $\mathbf{S}_f$ is one across face f and zero across any other faces. The normal component of $\mathbf{S}_f$ is continuous across the faces of adjacent elements, whereas the tangential component is not necessarily continuous. Moreover, it can be verified that the curl of an edge shape function is a linear combination of face shape functions:

$$\nabla \times \mathbf{N}_e = \sum_{f=1,F} C_{fe} \mathbf{S}_f \qquad (A.12)$$

where F is the number of faces of the mesh and $\underline{\mathbf{C}}$ is the $F \times E$ incidence matrix defined by[1]:

$$C_{fe} = \begin{cases} +1 \text{ if } f = \{m,n,l,i\} \text{ and } e = \{m,n\} \\ -1 \text{ if } f = \{m,n,l,i\} \text{ and } e = \{n,m\} \\ 0 \text{ otherwise} \end{cases} \qquad (A.13)$$

Notice that from (A.8) and (A.9) it follows that the edge element shape functions $\mathbf{N}_e$'s are linearly independent. Similarly, the face element shape function $\mathbf{S}_f$'s are linearly independent.

Moreover, the matrix $\underline{\mathbf{G}}$ represents the discretization of the gradient operator whereas the matrix $\underline{\mathbf{C}}$ the discretization of the curl operator:

$$\boldsymbol{j}(\mathbf{r}) = \sum_{k=1,NP} a_k N_k(\mathbf{r}) \Rightarrow \nabla \boldsymbol{j} = \sum_{e=1,E} (\underline{\mathbf{G}}\mathbf{a})_e \mathbf{N}_e \qquad (A.14)$$

$$\mathbf{U}(\mathbf{r}) = \sum_{e=1,E} b_e \mathbf{N}_e(\mathbf{r}) \Rightarrow \nabla \times \mathbf{U} = \sum_{f=1,F} (\underline{\mathbf{C}}\underline{\mathbf{b}})_f \mathbf{S}_f \qquad (A.15)$$

---

[1] The ordered sequence $\{m,n,l,i\}$ represents the face having m,n,l,i as nodes. Notice that any circular permutation represents the same face.

where $\underline{\mathbf{a}}$ and $\underline{\mathbf{b}}$ stand for the column vectors of numerical coefficients a_k and b_k.

The curl of $\mathbf{N}_e$ has the following expression:

$$\nabla \times \mathbf{N}_e = \nabla(s_e t_e) \times \nabla r_e \qquad \text{(A.16)}$$

The explicit expression for the gradient is obtained by the usual rules of partial differentiation, using the Jacobian matrix $\underline{\underline{\mathbf{J}}}$ of the transformation M:

$$\nabla r_e = \begin{bmatrix} \dfrac{\partial r_e}{\partial x} & \dfrac{\partial r_e}{\partial y} & \dfrac{\partial r_e}{\partial z} \end{bmatrix}^T = \underline{\underline{\mathbf{J}}}^{-1} \begin{bmatrix} \dfrac{\partial r_e}{\partial r_e} & \dfrac{\partial r_e}{\partial s_e} & \dfrac{\partial r_e}{\partial t_e} \end{bmatrix}^T = \underline{\underline{\mathbf{J}}}^{-1} \begin{bmatrix} 1 & 0 & 0 \end{bmatrix}^T$$

$$\text{(A.17)}$$

where

$$\underline{\underline{\mathbf{J}}} = \begin{bmatrix} \dfrac{\partial x}{\partial r_e} & \dfrac{\partial y}{\partial r_e} & \dfrac{\partial z}{\partial r_e} \\ \dfrac{\partial x}{\partial s_e} & \dfrac{\partial y}{\partial s_e} & \dfrac{\partial z}{\partial s_e} \\ \dfrac{\partial x}{\partial t_e} & \dfrac{\partial y}{\partial t_e} & \dfrac{\partial z}{\partial t_e} \end{bmatrix} = \begin{bmatrix} \mathbf{v}_1 & \mathbf{v}_2 & \mathbf{v}_3 \end{bmatrix} \qquad \text{(A.18)}$$

$$\underline{\underline{\mathbf{J}}}^{-1} = \frac{1}{\det(\mathbf{J})} \begin{bmatrix} \mathbf{v}_2 \times \mathbf{v}_3 & \mathbf{v}_3 \times \mathbf{v}_1 & \mathbf{v}_1 \times \mathbf{v}_2 \end{bmatrix} \qquad \text{(A.19)}$$

and the determinant of the Jacobian matrix is:

$$\det(\mathbf{J}) = \mathbf{v}_2 \times \mathbf{v}_3 \cdot \mathbf{v}_1 \qquad \text{(A.20)}$$

Cyclic permutations give the other gradients.

Appendix B: Tree-Cotree Decomposition

Solenoidality of the electric current dipole density $\mathbf{P}$ can be assured by introducing a vector potential $\mathbf{U}$, defined by

$$\mathbf{P} = \nabla \times \mathbf{U} \tag{B.1}$$

To assure the unicity of $\mathbf{U}$, an additional condition must be imposed. We prescribe the component of the vector potential along the direction determined by an arbitrarily chosen non-vanishing vector field $\mathbf{w}$ which does not possess closed field lines. The role played by this gauge condition is to eliminate all the irrotational fields from the functional space in which we search for the vector potentials. In other words, the gauge condition should constrain the null space of the discrete curl operator to be void [5].

We consider a simply connected region V_d and we express $\mathbf{U}$ and $\mathbf{P}$ using edge elements and face elements, respectively:

$$\mathbf{U}(\mathbf{r}) = \sum_{e=1,E} U_e \mathbf{N}_e(\mathbf{r}) \tag{B.2}$$

and

$$\mathbf{P}(\mathbf{r}) = \sum_{f=1,F} P_f \mathbf{S}_f(\mathbf{r}) \tag{B.3}$$

where $\mathbf{N}_e$'s are edge element shape functions and $\mathbf{S}_f$'s are face elements shape functions; consequently U_e and P_f are the degrees of freedom associated with the edge e and the face f.

From (B.1) and (B.2) we have:

$$\mathbf{P} = \sum_{e=1,E} U_e \nabla \times \mathbf{N}_e \tag{B.4}$$

and hence

$$\mathbf{P} = \sum_{e=1,E} \sum_{f=1,F} C_{fe} U_e \mathbf{S}_f \tag{B.5}$$

Equation (B.5) shows that the coefficients of (B.2) and (B.3) are linearly related:

$$\underline{\underline{C}}\,\underline{u} = \underline{p} \tag{B.6}$$

where $\underline{p}$ and $\underline{u}$ are the column vectors of coefficients P_f and U_e, respectively.

The relationship (B.6) can be regarded as a linear system where $\underline{u}$ and $\underline{p}$ play the roles of unknowns and right hand side, respectively.

The existence of a solution for system (B.6) is subject to the compatibility condition, which requires that $\underline{p}$ correspond to a solenoidal vector field. If the

system is compatible, the solution is not unique. In fact, from (A.10) and (A.12) it turns out that:

$$0 = \nabla \times \nabla N_k = \sum_{f=1,F} \left(\underline{\underline{CG}}\right)_{fk} \mathbf{S}_f \tag{B.7}$$

thus[1],

$$\underline{\underline{CG}} = \underline{0} \tag{B.8}$$

because the shape functions $\mathbf{S}_f$ are linearly independent (see Appendix A). From (B.8) it follows that adding any linear combination of columns of $\underline{G}$ to $\underline{u}$ is still a solution of (B.6); in fact, the columns of $\underline{G}$ yield irrotational vector potential (and zero dipole densities) [3]. Thus, in this case, imposing the gauge condition is equivalent to the problem of assuring uniqueness for system (B.6).

Let us consider the oriented graph formed by the nodes and oriented edges of the edge element mesh. $\underline{G}$ and $\underline{C}$ are the edge-node and face-edge incidence matrices. From graph theory, the rank of the $E \times NP$ matrix $\underline{G}$ is NP-1 while the rank of the $F \times E$ matrix $\underline{C}$ is $E-NP+1$. The uniqueness of the solution of (B.6) is guaranteed if $\mathbf{U}$ in (B.2) is represented by $E-NP+1$ degrees of freedom.

To select the proper degrees of freedom, we notice that the uniqueness of the solution of (B.6) means that $\nabla \times \mathbf{U} \neq \mathbf{0}$ when at least one of the $E-NP+1$ degrees of freedom is different from zero. Let us decompose the graph into an arbitrary tree (NP-1 edges) and cotree (the residual E-NP+1 edges) (the algorithm to identify all possible trees of a graph is presented in [6]). Then, assuming U_e=0 when e is an edge of the tree, we notice that $\nabla \times \mathbf{U} \neq \mathbf{0}$ if at least one degree of freedom related to a cotree edge is different from zero. In fact, each edge of the cotree closes a single independent loop $\boldsymbol{g}_e$ with the edges of the tree and the circulation of $\mathbf{U}$ along $\boldsymbol{g}_e$ is equal to $\pm U_e$ ($\boldsymbol{g}_e$ does not include cotree edges apart from edge e). Therefore, the $E-NP+1$ degrees of freedom associated to the edges of the cotree lead to a reduced set of equations that, if compatible, admit a unique solution [5, 7, 8].

For the sake of completeness, it is worth noting that the NP-1 degrees of freedom associated to the tree edges can be used to represent gradient vector fields. In fact, once the degrees of freedom of the edges of the tree have been assigned, for any cotree edge e we choose U_e so that the circulation of $\mathbf{U}$ along $\boldsymbol{g}_e$ is equal to zero (since the circulation of $\mathbf{U}$ along $\boldsymbol{g}_e$ involves only the cotree edge e, we find that U_e depends linearly on the degrees of freedom associated to the tree edges). Therefore, (B.2) gives a vector field $\mathbf{U}$ that is irrotational.

---

[1] Notice that (B.8) is the discrete equivalent of $\nabla \times \nabla f$=0.

Appendix C: Integration of the hyper-singular term

Here equation (3.15) is proven.

First we notice that the hyper-singular term $k^{-2}\nabla\nabla g_0(\mathbf{r}\,|\,\mathbf{r}')$ is a distribution (see [9]). This distribution acts on vector fields in the following way:

$$\frac{1}{k^2}\nabla\nabla g_0(\mathbf{r}\,|\,\mathbf{r}'):\mathbf{w}(\mathbf{r}) \rightarrow \frac{1}{k^2}\nabla\left\{\nabla\cdot\left[\int g_0(\mathbf{r}\,|\,\mathbf{r}')\mathbf{w}(\mathbf{r})d\mathbf{r}\right]\right\} \tag{C.1}$$

The definition of the elements of $\mathbf{L}_0^S$ is:

$$\left(\mathbf{L}_0^S\right)_{ij} = \frac{\boldsymbol{m}_0}{k^2}\int_{\Omega_f}\mathbf{P}_i(\mathbf{r})\cdot\nabla\left\{\nabla\cdot\left[\int_{\Omega_f}g_0(\mathbf{r}\,|\,\mathbf{r}')\cdot\mathbf{P}_j(\mathbf{r}')d\mathbf{r}'\right]\right\}d\mathbf{r}. \tag{C.2}$$

Then, taking into account that $\nabla\cdot\mathbf{P}_i = 0$ and applying the divergence theorem w.r.t. the outer most integral, it turns out that:

$$\begin{aligned}
\left(\mathbf{L}_0^S\right)_{ij} &= \frac{\boldsymbol{m}_0}{k^2}\int_{\Omega_f}\mathbf{P}_i(\mathbf{r})\cdot\nabla\left\{\nabla\cdot\left[\int_{\Omega_f}g_0(\mathbf{r}\,|\,\mathbf{r}')\cdot\mathbf{P}_j(\mathbf{r}')d\mathbf{r}'\right]\right\}d\mathbf{r} \\
&= \frac{\boldsymbol{m}_0}{k^2}\int_{\Omega_f}\nabla\cdot\left\{\mathbf{P}_i(\mathbf{r})\nabla\cdot\left[\int_{\Omega_f}g_0(\mathbf{r}\,|\,\mathbf{r}')\cdot\mathbf{P}_j(\mathbf{r}')d\mathbf{r}'\right]\right\}d\mathbf{r} \\
&= \frac{\boldsymbol{m}_0}{k^2}\oint_{\partial\Omega_f}\hat{\mathbf{n}}(\mathbf{r})\cdot\mathbf{P}_i(\mathbf{r})\nabla\cdot\left[\int_{\Omega_f}g_0(\mathbf{r}\,|\,\mathbf{r}')\cdot\mathbf{P}_j(\mathbf{r}')d\mathbf{r}'\right]dS(\mathbf{r}) \\
&= \frac{\boldsymbol{m}_0}{k^2}\oint_{\partial\Omega_f}\hat{\mathbf{n}}(\mathbf{r})\cdot\mathbf{P}_i(\mathbf{r})\int_{\Omega_f}\nabla\cdot\left[g_0(\mathbf{r}\,|\,\mathbf{r}')\cdot\mathbf{P}_j(\mathbf{r}')\right]d\mathbf{r}'dS(\mathbf{r})
\end{aligned} \tag{C.3}$$

where $\hat{\mathbf{n}}(\mathbf{r})$ stands for the outward normal at point $\mathbf{r}$ of Ω_f.

Then, we notice that[1]

$$\nabla\cdot\left[g_0(\mathbf{r}\,|\,\mathbf{r}')\mathbf{P}_j(\mathbf{r}')\right] = -\nabla'\cdot\left[g_0(\mathbf{r}\,|\,\mathbf{r}')\mathbf{P}_j(\mathbf{r}')\right] \tag{C.4}$$

as follows by taking into account the solenoidality of $\mathbf{P}_j$ and that g_0 is a function of **r-r'**. Finally, replacing (C.4) in (C.3) and applying the divergence theorem w.r.t. the inner most integral we get:

---

[1] As usual, the symbol ∇ refers to the spatial co-ordinates **r** while ∇' refers to the spatial co-ordinates **r'**.

$$\left(\mathbf{L}_0^S\right)_{ij} = -\frac{m_0}{k^2} \int\limits_{\partial\Omega_f} \int\limits_{\partial\Omega_f} \hat{\mathbf{n}}(\mathbf{r}) \cdot \mathbf{P}_i(\mathbf{r})\, g_0(\mathbf{r}\,|\,\mathbf{r}')\, \hat{\mathbf{n}}(\mathbf{r}') \cdot \mathbf{P}_j(\mathbf{r}')\, \mathrm{d}S(\mathbf{r}')\mathrm{d}S(\mathbf{r}) \qquad \text{(C.5)}$$

Appendix D: Programming the finite element code

List of symbols

I_m^{CE}	set of indices of the cotree edges lying on the boundary of element m
$\tilde{I}_{\tilde{m}}^{CE}$	set of indices of the cotree edges lying on the boundary surface $\tilde{m}$
N_{bf}	no. of boundary faces of the mesh (boundary faces are numbered fro 1 to N_{bf})
N_{CE}	no. of cotree edges of the mesh (the cotree edges are numbered from 1 to N_{CE})
N_e	no. of elements of the mesh (the elements are numbered from 1 to N_e)
N_{edges}	no. of edges of the mesh (the edges are numbered from 1 to N_{edges})
N_p	no. of nodes of the mesh (the nodes are numbered from 1 to N_p)
N_G	no. of Gauss points per element
$\tilde{N}_G$	no. of Gauss points per face
$\mathbf{r}_n^m$	n-th Gauss point in the element m
$\tilde{\mathbf{r}}_n^{\tilde{m}}$	n-th Gauss point on face $\tilde{m}$
$\Sigma_{\tilde{m}}$	surface of the $\tilde{m}$-th boundary face of the mesh
$\boldsymbol{t}_m$	three dimensional domain occupied by element m
$vol(\boldsymbol{t}_m)$	volume of element m
w_n	Gauss weight at the n-th point of the master element $[-1, 1]\times[-1, 1]\times[-1, 1]$

Assembling $\underline{\mathbf{V}}$, $\underline{\underline{\mathbf{R}}}$, $\underline{\underline{\mathbf{L}}}$, $\underline{\underline{d\mathbf{L}}}$, $\underline{\mathbf{L}}_0$ and $\underline{\underline{\mathbf{L}}}_0^S$

The integrals appearing in the numerical formulation can be written in the following way:

$$\left(\underline{\mathbf{V}}^{(i)}\right)_k = \sum_{m=1}^{N_e} \boldsymbol{n}_{m,k}$$
(1)

$$\left(\underline{\underline{\mathbf{R}}}\right)_{kj} = \sum_{m=1}^{N_e} \boldsymbol{r}_{m,k,j}$$
(2)

$$\left(\underline{\underline{\mathbf{L}}}\right)_{kj} = \sum_{m=1}^{N_e} \sum_{l=1}^{N_e} \boldsymbol{a}_{m,l,k,j}$$
(3)

where N_e is the number of elements of the mesh,

$$\boldsymbol{n}_{m,k} \triangleq \int_{t_m} \nabla \times \mathbf{N}_k(\mathbf{r}) \cdot \mathbf{E}^{(i)}(\mathbf{r}) d\mathbf{r}$$
(4)

$$\boldsymbol{r}_{m,k,j} \triangleq \frac{1}{\boldsymbol{s}_f - \boldsymbol{s}_0} \int_{t_m} \nabla \times \mathbf{N}_k(\mathbf{r}) \cdot \nabla \times \mathbf{N}_j(\mathbf{r}) d\mathbf{r}$$
(5)

$$\boldsymbol{a}_{m,l,k,j} \triangleq \boldsymbol{m}_0 \int_{t_m} \int_{t_l} \nabla \times \mathbf{N}_k(\mathbf{r}) \cdot \mathbf{G}^{ee}(\mathbf{r} \mid \mathbf{r'}) \cdot \nabla \times \mathbf{N}_j(\mathbf{r'}) d\mathbf{r'} d\mathbf{r}.$$
(6)

and $\boldsymbol{t}_m$ is the three dimensional domain of the m-th element of the finite element mesh.

The standard procedure for assembling $\underline{\mathbf{V}}$, $\underline{\underline{\mathbf{R}}}$ and $\underline{\underline{\mathbf{L}}}$, assuming that the non-singular integrals (4) and (5) are computed by the Gauss quadrature method, is given by the following algorithms (N_G is the number of Gauus points per element, I_m^{CE} is the set of indices of the cotree edges lying on the boundary of element m):

Procedure 1 : compute and store the values of the shape functions assumed in the Gauss points for any element

    for *m=1, ..., N_e*
        for $k \in I_m^{CE}$
            for *n=1, ...,N_G*
                set $SHPF(m,k,n) = \nabla \times \mathbf{N}_k\left(\mathbf{r}_n^m\right)$[1];

---

[1] For given *m*, *k* and *n*, SHPF(m,k,n) is a three component vector.

Procedure 2 : compute $\underline{\mathbf{V}}$

> set $\underline{\mathbf{V}}=\underline{\mathbf{0}}$;
> for $m=1, ..., N_e$
>> for $n=1, ..., N_G$
>>> for $k \in I_m^{CE}$
>>>> $\boldsymbol{n}_{n,m,k} = \mathbf{E}^{(i)}(\mathbf{r}_n^m) \cdot SHPF(m,k,n) w_n vol(\boldsymbol{t}_m);$
>>>> $(\underline{\mathbf{V}}^{(i)})_k = (\underline{\mathbf{V}}^{(i)})_k + \boldsymbol{n}_{n,m,k};$

Procedure 3 : compute $\underline{\mathbf{R}}$[1]

> set $\underline{\mathbf{R}}=\underline{\mathbf{0}}$;
> for $m=1, ..., N_e$
>> for $n=1, ..., N_G$
>>> for $k \in I_m^{CE}$
>>>> for $j \in I_m^{CE}$ and $j \leq k$
>>>>> $\boldsymbol{r}_{n,m,k,j} = SHPF(m,k,n) \cdot SHPF(m,k,n) w_n vol(\boldsymbol{t}_m)/8;$
>>>> $(\underline{\underline{\mathbf{R}}})_{kj} = (\underline{\underline{\mathbf{R}}})_{kj} + \boldsymbol{r}_{n,m,k,j};$
> set $(\underline{\underline{\mathbf{R}}})_{jk} = (\underline{\underline{\mathbf{R}}})_{kj}$ for $j < k;$
> set $\underline{\underline{\mathbf{R}}} = \dfrac{1}{\boldsymbol{s}_f - \boldsymbol{s}_0} \underline{\underline{\mathbf{R}}};$

Procedure 4 : compute $\underline{\underline{\mathbf{L}}}$ [2]

> set $\underline{\underline{\mathbf{L}}}=\underline{\mathbf{0}}$;
> for $m=1, ..., N_e$
>> for $l=1, ..., N_e$
>>> *compute and store any quantity that depends only on m and l*[3];
>>> for $k \in I_m^{CE}$
>>>> for $j \in I_l^{CE}$ and $j \leq k$
>>>>> **call** *compute* $\boldsymbol{a}_{m,l,k,j};$
>>>>> $(\underline{\underline{\mathbf{L}}})_{kj} = (\underline{\underline{\mathbf{L}}})_{kj} + \boldsymbol{a}_{m,l,k,j};$
> set $(\underline{\underline{\mathbf{L}}})_{jk} = (\underline{\underline{\mathbf{L}}})_{kj}$ for $j \leq k;$

Notice that procedure 4 is valid for computing $\underline{\underline{d\mathbf{L}}}$ and $\underline{\mathbf{L}}_0$ also. In the first case $\boldsymbol{a}_{m,l,k,j}$ has to be replaced by $\boldsymbol{da}_{m,l,k,j}$ defined as

---

[1] The matrix R is sparse.

[2] As example, compute and store $\mathbf{G}^{ee}(\mathbf{r}_i^m \mid \mathbf{r}_{i'}^l)$ for $i,i'=1, ...,N_G$

[3] The algorithm for computing $\boldsymbol{a}_{m,l,k,j}$ is left to the reader (see [8] for the case of static scalar Green function).

$$\boldsymbol{da}_{m,l,k,j} \triangleq \boldsymbol{m}_0 \iint\limits_{\boldsymbol{t}_m \boldsymbol{t}_l} \nabla \times \mathbf{N}_k(\mathbf{r}) \cdot \boldsymbol{d}\mathbf{G}^{ee}(\mathbf{r} \mid \mathbf{r}') \cdot \nabla \times \mathbf{N}_j(\mathbf{r}') d\mathbf{r}' d\mathbf{r} \,,$$

(7)

whereas in the second case $\boldsymbol{a}_{m,l,k,j}$ has to be replaced by $\boldsymbol{a}_{m,l,k,j}^0$ defined as

$$\boldsymbol{a}_{m,l,k,j}^0 \triangleq \boldsymbol{m}_0 \iint\limits_{\boldsymbol{t}_m \boldsymbol{t}_l} \nabla \times \mathbf{N}_k(\mathbf{r}) \cdot g_0(\mathbf{r} \mid \mathbf{r}') \nabla \times \mathbf{N}_j(\mathbf{r}') d\mathbf{r}' d\mathbf{r}$$

(8)

The numerical computation of $\boldsymbol{da}_{m,l,k,j}$ can be carried out by Gauss quadrature rule, whereas the numerical computation of $\boldsymbol{a}_{m,l,k,j}^0$ can be carried out by taking into account (3.16). Specifically, the term arising from $\dfrac{jk}{4\boldsymbol{p}} e^{jk|\mathbf{r}-\mathbf{r}'|/2} \mathrm{sinc}\left(\dfrac{k|\mathbf{r}-\mathbf{r}'|}{2}\right)$ can be computed by the Gauss quadrature rule, whereas the term arising from $\dfrac{1}{4\boldsymbol{p}|\mathbf{r}-\mathbf{r}'|}$ can be computed by the approach proposed in [8].

Finally, the surface integral (3.15) can be written as:

$$\left(\underline{\underline{\mathbf{L}}}_0^S\right)_{kj} = \sum_{\tilde{m}=1}^{N_{bf}} \sum_{\tilde{l}=1}^{N_{bf}} \boldsymbol{b}_{\tilde{m},\tilde{l},k,j}$$

(9)

where N_{bf} is the number of boundary faces of the mesh,

$$\boldsymbol{b}_{\tilde{m},\tilde{l},k,j} \triangleq -\frac{\boldsymbol{n}_0}{k^2} \iint\limits_{\Sigma_{\tilde{m}} \Sigma_{\tilde{l}}} \hat{\mathbf{n}}(\mathbf{r}) \cdot \nabla \times \mathbf{N}_k(\mathbf{r}) \, g_0(\mathbf{r} \mid \mathbf{r}') \, \hat{\mathbf{n}}(\mathbf{r}') \cdot \nabla \times \mathbf{N}_j(\mathbf{r}') dS(\mathbf{r}') dS(\mathbf{r})$$

(10)

and Σ_m is the m-th boundary face. The algorithm for computing $\underline{\underline{\mathbf{L}}}_0^S$ is ($\tilde{I}_{\tilde{m}}^{CE}$ is the set of indices of cotree edges lying on the boundary surface $\tilde{m}$):

<u>Procedure 5</u> : compute $\underline{\underline{\mathbf{L}}}_0^{S\,\mathbf{1}}$

   set $\underline{\underline{\mathbf{L}}}_0^S = \underline{\underline{\mathbf{0}}}$;
   compute and store the values of $\hat{\mathbf{n}}(\mathbf{r}) \cdot \nabla \times \mathbf{N}_k(\mathbf{r})$ *evaluated at the Gauss points of any boundary face;*
   for $\tilde{m} = 1, \ \ldots, N_{bf}$

---

[1] The algorithm for computing $\boldsymbol{b}_{\tilde{m},\tilde{l},k,j}$ is left to the reader (for instance, combine (3.16) with (18) and (19) in [8]).

$\qquad$ **for** $\tilde{l} = 1, \ldots, N_{bf}$

$\qquad\qquad$ *compute and store any quantity that depends only on $\tilde{m}$ and $\tilde{l}$* [1];

$\qquad\qquad$ **for** $k \in \tilde{I}_{\tilde{m}}^{CE}$

$\qquad\qquad\qquad$ **for** $j \in \tilde{I}_{\tilde{l}}^{CE}$ *and* $j \le k$

$\qquad\qquad\qquad\qquad$ **call** *compute* $\boldsymbol{b}_{\tilde{m},\tilde{l},k,j}$;

$$\left(\underline{\underline{\mathbf{L}}}_0^S\right)_{kj} = \left(\underline{\underline{\mathbf{L}}}_0^S\right)_{kj} + \boldsymbol{b}_{\tilde{m},\tilde{l},k,j} ;$$

$\qquad$ **set** $\left(\underline{\underline{\mathbf{L}}}_0^S\right)_{jk} = \left(\underline{\underline{\mathbf{L}}}_0^S\right)_{kj}$ *for* $j \le k$;

We notice that the volume and surface integrals are carried out on the master element [-1, 1]×[-1, 1]×[-1, 1] or the master face [-1, 1]×[-1, 1], respectively. The Gauss weight refer to the master element or face; the Gauss points for a generic element or face are obtained as image under the transformation *M* of the Gauss points for the master element and face, respectively.

---

[1] As example, compute and store $g_0\left(\tilde{\mathbf{r}}_i^{\tilde{m}} \mid \tilde{\mathbf{r}}_{i'}^{\tilde{l}}\right)$ for *i,i'=1, …, $\tilde{N}_G$*

The incidence matrices and other relevant geometrical and topological data

<u>Input</u>

$\mathbf{x}(i, 1:3)$, $i=1:N_p$	coordinates of the i-th nodal point
$\mathbf{ix}(\text{i}, j)$, $i=1:8$, $j=1:N_e$	label of the i-th node of the j-th element (see fig 2)
$\mathbf{ix}(9, j)$, $j=1: N_e$	label of the material properties of the j-th element

<u>Output</u>

$\mathbf{ixb}(i, j)$, $i=1:4$, $j=1:N_{bf}$	label of the i-th node of the j-th boundary face
$\mathbf{ltact}(i, j)$, $i=1:12$, $j=1:N_e$	label of the i-th cotree edge of the j-th element. $\mathbf{ltact}(i,j)$ is zero if the i-th edge belongs to the tree.
$\mathbf{ltact\_bou}(i, j)$, $i=1:4$, $j=1:N_{bf}$	label of the i-th cotree edge of the j-th boundary face. $\mathbf{ltact\_bou}(i, j)$ is zero if the i-th edge belongs to the tree.
$\mathbf{inc}(1, j)$, $\mathbf{inc}(2, j)$, $j=1:N_{edges}$	labels of the two nodes identifying the j-th edge
$\mathbf{ncoalb}(i)$, $i=1:N_{CE}$	label of the i-th edge of the co-tree
$\mathbf{latel}(i, j)$, $i=1:12$, $j=1:N_e$	label of the i-th edge of the j-th element (see fig 2)
$\mathbf{ielface}(j)$, $j=1:N_{bf}$	label of the element of the j-th boundary face
$\mathbf{indface}(i, j)$, $i=1:4$, $j=1: N_{bf}$	(local) label of the i-th edge of the j-th boundary face (see fig. 2)

<u>Procedure 1</u> : find boundary faces (N_{bf}, $\mathbf{ixb}$, $\mathbf{ielface}$ and $\mathbf{indface}$)

j=0;
for $i_{el1}=1, ..., N_e$
    for *each face j_{f1} of element i_{el1}*
        set *ind=false;*
        while *ind=false*
            for $i_{el2}= i_{el1}+1, ..., N_e$
                for *each face j_{f2} of element i_{el2}*
                    if $j_{f1}=j_{f2}$ **set** *ind=true;*[1]
        if *ind=false*
           j=j+1;
           insert the nodes of face j_{f1} in the list $\mathbf{ixb}(1:4, j)$;
           insert i_{el1} in the list $\mathbf{ielface}(j)$;
           insert j_{f1} in the list $\mathbf{indface}(1:4, j)$;
$N_{bf}=j;$

---

[1] $j_{f1}=j_{f2}$ means that the set of nodes of face j_{f1} is equal to the set of nodes of face j_{f2}.

Procedure 2 :   compute the incidence matrix (N_{edges}, **inc**)

lat=0;
for i_{el}*=1, ..., N_e*
    for *each edge i (i=1, ..., 12) of element i_{el}*
        set *ind=false;*
        if *edge i is already in **inc**[1]*
        then set ***latel**(i, i_{el})=position where edge i occurs in **inc**;*
        else
            lat=lat+1;
            *insert the label of nodes corresponding to edge i in **inc**(:, lat);*
            ***latel**(i, i_{el})=lat;*
N_{edges}*=lat;*

Procedure 3 :   compute **ltact**[2]

for *each element i_{el}*
    for *each edge i (i=1, ..., 12) of element i_{el}*
        lat=latel(i,i_{el});
        if *lat belong to the co-tree **then set** ltact(i, i_{el})=lat;*
        else *ltact(i, i_{el})=0;*

Procedure 4 :   compute **ltact_bou**

for *each boundary face j_f*
    for *each edge i (i=1, ..., 4) of the face j_f*
        i_{el}=ielface(j_f);
        ilat=indface(i,j_f);
        lat=ltact(ilat,i_{el});
        ltact_bou(i,j_f)=lat;

---

[1] This test consists in searching the column of **inc** containing the nodes related to edge *i*.
[2] Notice that the procedure for the tree-cotree decomposition is described in [6]. The input of this procedure is the incidence matrix **inc** and the output is the list of co-tree edges **ncoalb**.

References

[1] J. R. Bowler, S. A. Jenkins, L. D. Sabbagh, H. A. Sabbagh (1991) "Eddy-Current probe impedante due to a volumetric flaw" J. Appl. Phys., vol 70, no. 3, 1107-1114.

[2] Chen-To Tai (1993) Dyadic Green Functions in Electromagnetic Theory, 2nd ed., New York: IEEE Press.

[3] A. Bossavit (1998) *Computational Electromagnetism* Boston: Academic Press.

[4] J.S. van Welij (1985) "Calculation of eddy currents in terms of H on hexahedra", *IEEE Trans. Magn.* 21, 2239-2241.

[5] R. Albanese and G. Rubinacci (1998) "Finite element methods for the solution of 3D eddy current problems" *in Advances in Imaging and Electron Physics*, Academic Press, Vol. 102, pp. 1-86.

[6] H. W. Hale (1961) "A logic for identifying the trees of a graph", *Trans. AIEE*, PAS-80, 195-198.

[7] R. Albanese and G. Rubinacci (1998) "Solution of three dimensional eddy current problems by integral and differential methods", *IEEE Trans Magn.* 24, 98-101.

[8] R. Albanese and G. Rubinacci (1988) "Integral formulation for 3D eddy-current computation using edge elements", *IEE Proc.*, Vol. 135, Pt. A, 457-462.

[9] W. C. Chew (1995) *Waves and fields in inhomogeneous media* New York: IEEE Press.